



HAL
open science

Introducing hysteresis in snow depletion curves to improve the water budget of a land surface model in an Alpine catchment

Claire Magand, Agnès Ducharne, Nicolas Le Moine, Simon Gascoin

► To cite this version:

Claire Magand, Agnès Ducharne, Nicolas Le Moine, Simon Gascoin. Introducing hysteresis in snow depletion curves to improve the water budget of a land surface model in an Alpine catchment. *Journal of Hydrometeorology*, 2014, 15 (2), pp.631-649. 10.1175/JHM-D-13-091.1 . hal-00927632v1

HAL Id: hal-00927632

<https://hal.science/hal-00927632v1>

Submitted on 13 Jan 2014 (v1), last revised 29 Aug 2014 (v2)

HAL is a multi-disciplinary open access archive for the deposit and dissemination of scientific research documents, whether they are published or not. The documents may come from teaching and research institutions in France or abroad, or from public or private research centers.

L'archive ouverte pluridisciplinaire **HAL**, est destinée au dépôt et à la diffusion de documents scientifiques de niveau recherche, publiés ou non, émanant des établissements d'enseignement et de recherche français ou étrangers, des laboratoires publics ou privés.



AMERICAN METEOROLOGICAL SOCIETY

Journal of Hydrometeorology

EARLY ONLINE RELEASE

This is a preliminary PDF of the author-produced manuscript that has been peer-reviewed and accepted for publication. Since it is being posted so soon after acceptance, it has not yet been copyedited, formatted, or processed by AMS Publications. This preliminary version of the manuscript may be downloaded, distributed, and cited, but please be aware that there will be visual differences and possibly some content differences between this version and the final published version.

The DOI for this manuscript is doi: 10.1175/JHM-D-13-091.1

The final published version of this manuscript will replace the preliminary version at the above DOI once it is available.

If you would like to cite this EOR in a separate work, please use the following full citation:

Magand, C., A. Ducharne, N. Le Moine, and S. Gascoin, 2013: Introducing hysteresis in snow depletion curves to improve the water budget of a land surface model in an Alpine catchment. *J. Hydrometeor.* doi:10.1175/JHM-D-13-091.1, in press.



1 **Introducing hysteresis in snow depletion curves to improve the**
2 **water budget of a land surface model in an Alpine catchment**

3 **CLAIRE MAGAND ***, AGNÈS DUCHARNE, NICOLAS LE MOINE

UMR-SISYPHE, UPMC/CNRS, Paris, France

AND SIMON GASCOIN

CESBIO, Toulouse, France

* *Corresponding author address:* Claire Magand, UMR Sisyphe, CNRS/UPMC

Case 105, 4 Place Jussieu, 75005 Paris, France.

E-mail: claire.magand@upmc.fr

ABSTRACT

4
5 The Durance watershed (14 000 km²), located in the French Alps, generates 10% of
6 French hydro-power and provides drinking water to 3 million people. The Catchment Land
7 Surface Model (CLSM), a distributed land surface model (LSM) with a multilayer, physically-
8 based snow model, has been applied in the upstream part of this watershed where snowfall
9 accounts for 50% of the precipitation. The CLSM subdivides the upper Durance watershed,
10 where elevations range from 800 m to 4000 m within 3580 km², into elementary catchments
11 with an average area of 500 km². We first show the difference between the dynamics of
12 the accumulation and ablation of the snow cover using MODIS images and snow depth
13 measurements. The extent of snow cover increases faster during accumulation than during
14 ablation because melting occurs at preferential locations. This difference corresponds to
15 the presence of a hysteresis in the snow cover depletion curve of these catchments, and we
16 adapted the CLSM by implementing such a hysteresis in the snow cover depletion curve of the
17 model. Different simulations were performed to assess the influence of the parameterizations
18 on the water budget and the evolution of the extent of the snow cover. Using 6 gauging
19 stations, we demonstrate that introducing a hysteresis in the snow cover depletion curve
20 improves melting dynamics. We conclude that our adaptation of the CLSM contributes to a
21 better representation of snowpack dynamics in a LSM that enables mountainous catchments
22 to be modeled for impact studies such as those of climate change.

1. Introduction

A strong positive feedback on climate comes from the surface albedo, especially over snow-covered areas characterized by a high reflectivity. Snow cover is also responsible for the strong seasonal contrasts observed in the hydrological regimes of mountainous and high latitude regions. During winter, snow cover acts as a water reservoir where snowfall accumulates. A large quantity of water is subsequently released during the melt season. Modeling snow cover is therefore crucial for the accurate simulation of both the energy and water budgets.

During the last three decades, major efforts have been made by the Land Surface Models community to better describe snowpack physics by increasing vertical resolution and complexifying snow parameterizations. Such improvements led to better ground thermodynamics at the continental scale (Loth and Graf 1998; Stieglitz et al. 2001a), but difficulties in simulating the timing of snowpack ablation remained (Pomeroy et al. 1998; Slater et al. 2001). Accounting for the sub-grid variability of the snow-cover extent is important because it modifies the energy and water budgets via its effect on the mean albedo, but also because it changes the dynamics of fluxes related to the presence of snow on the grid cell (e.g., sublimation and melt). Many snow cover depletion curves (SCDs) relating the snow cover fraction (SCF) of a grid cell to the average snow depth or snow water equivalent (SWE) were introduced to account for the horizontal variability of the snow cover within a LSM's grid cell (Gray and Male 1981; Hansen et al. 1983; Verseghy 1991; Douville et al. 1995; Yang et al. 1997; Roesch et al. 2001; Essery and Pomeroy 2004). The sophistication of these SCDs has increased over the years, from a linear equation limited by an SWE threshold (Verseghy 1991; Sellers et al. 1996) applied to all types of vegetation to more complex algorithms accounting for vegetation properties, wind effects, or ground roughness length (D ery et al. 2004; Livneh et al. 2010; Wang 2012).

At a small scale (26 ha), Luce and Tarboton (2004) highlighted the existence of a hysteresis in the SCD with different dynamics between accumulation and ablation periods. During accumulation the snow-cover extent quickly reaches full-coverage, after which the snowpack

50 increases homogeneously in depth. In contrast, snow melts from preferential locations dur-
51 ing ablation, leading to heterogeneous patterns. Liston (2004) also developed a sub-grid
52 snow distribution to describe these two different processes and validated this method at the
53 mesoscale (2500 km²). More recently, Niu and Yang (2007) and Dutra et al. (2010) intro-
54 duced a hysteresis in the SCD by inversely relating the snow-cover area to the snowpack
55 bulk density: as the snow density increases with respect to the snow age, the snow-cover
56 area for a given quantity of snow gets lower later in the snow season. Although this study
57 showed good consistency with satellite images of snow cover at a global scale (10000 km²),
58 we consider with Swenson and Lawrence (2012) that the observed hysteresis is more likely
59 due to the variability of topography or vegetation within the catchment than to the age of
60 snow.

61 The Catchment Land Surface Model (CLSM) is an LSM developed by Koster et al.
62 (2000) and Ducharne et al. (2000) to generate water and energy fluxes between land surfaces
63 and the atmosphere in General Circulation Models (GCMs) in which a multilayer, physically
64 based snow scheme is included (Lynch-Stieglitz 1994). We applied this model in the Durance
65 watershed (approximately 14 000 km²) located in the southern French Alps with an altitude
66 range of 4000 meters (cf. Figure 1). We focus on the upper catchment part, which provides
67 40% of the discharge at the outlet of the Durance watershed and where snowfall accounts
68 for more than 50% of the total precipitation. A correct estimation of the water resource
69 and its evolution under climate change is particularly important as 10% of French hydro-
70 power is produced in the Durance watershed (Figure 1) and it supplies drinking water to
71 approximately 3 million people.

72 The CLSM subdivides the domain into elementary catchments, here with an average area
73 of 500 km² (Figure 1b). Topography, vegetation and aspect (north-facing or south-facing)
74 are highly variable within each elementary catchment in the Upper Durance watershed and
75 these three features play a key role in producing heterogeneous snow cover, especially during
76 melting events (Gray and Male 1981; Lundberg et al. 1998; Essery and Pomeroy 2004; Liston

77 2004; Swenson and Lawrence 2012). Hence, the extent of the snow cover should vary within
78 each catchment and impact the time and rate of melt. Therefore, the objectives of this study
79 were first to investigate whether or not there is an hysteresis in the observed relationship
80 between SCF and SWE using MODIS images and snow depth measurements, and then to
81 assess the influence of the SCF parameterizations on the simulated water budget in the
82 context of an Alpine environment.

83 2. Characterization of the observed hysteresis

84 The Upper Durance River watershed was subdivided into eight elementary catchments of
85 about 500 km² for the requirements of the model (Section 3). A 25-m DEM produced by the
86 French National Geographic Institute (IGN) was used to delineate the catchments. Account-
87 ing for the locations of the gauging stations was also important to delineate the catchments so
88 that the simulations could be validated with observations. Eventually, lithological data from
89 the French Geological Survey (BRGM) were collected to ensure that hydrological catchments
90 were homogeneous in terms of soil characteristics. Table 1 summarizes the characteristics of
91 each catchment.

92 *a. Snow-cover area and snow depth datasets*

93 SCFs were calculated from mid-resolution images of snow cover extent provided by
94 MOD10A2 (cf. [http://nsidc.org/data/docs/daac/modis_v5/mod10a2_modis_terra_snow_](http://nsidc.org/data/docs/daac/modis_v5/mod10a2_modis_terra_snow_8-day_global_500m_grid.gd.html)
95 [8-day_global_500m_grid.gd.html](http://nsidc.org/data/docs/daac/modis_v5/mod10a2_modis_terra_snow_8-day_global_500m_grid.gd.html)), an eight-day composite snow product from the Moderate-
96 Resolution Imaging Spectroradiometer (MODIS). Snow-cover and cloud-cover extents are
97 given as binary information in 500-m pixels from April 2000 to February 2012. A pixel is
98 labeled as 'snow-covered' if snow was observed on at least once ; a pixel is labeled as 'clouded'
99 if the cell was obscured during all observation days (Riggs et al. 2006). The SCF and cloud
100 cover fraction of each catchment were extracted from these images using GIS tools. Cloud

101 cover can significantly reduce snow-cover extent measurements. Therefore, we excluded im-
102 ages where 10% of the catchment was cloud covered, which corresponded to 6% of each time
103 series. Note also that the SCFs of catchment 2 were not taken into account in this study be-
104 cause MODIS SCFs seem to overestimate the snow cover area in this catchment (indicating
105 snow even in summer), most likely because of the presence of glaciers (approximately 20%
106 of the catchment area). We did not consider MODIS observations on a daily timescale as
107 previous studies have demonstrated that approximately 60% of the images are obscured by
108 clouds in the Alps (Parajka et al. 2006; Picouet 2012).

109 To characterize the empirical SCD, snow depth data were also collected from the BD-
110 CLIM (Base de Données Climatologiques), a dataset produced by Météo-France, the French
111 national weather service. Snow depth measurements were obtained from 89 stations located
112 in the Upper Durance. Most of these stations, however, do not provide useful information
113 because of too many gaps and we used only 35 stations, providing measurements between
114 April 2000 and March 2006 (Figure 1). The number of stations used in each catchment is
115 indicated in Table 1. In catchments 1, 3 and 6, the elevation of these stations is well dis-
116 tributed within the elevation range of the catchment they belong to (Figure 1). We mainly
117 show results from catchment 3 in this article because it is the best instrumented with 10
118 stations, the elevation of which range from 1355 to 2630 meters while catchment elevations
119 range from 892 to 3357 m. This is not the case in the other catchments where the stations are
120 located around the same elevation. In catchment 4 for instance, there are only two stations
121 gathered along the streams, both being at an elevation of about 1200 m (Figure 1). Snow
122 depths measurements were averaged over each catchment to get a mean snow depth time
123 series. The consequences of this averaging in catchments where the snow depth stations are
124 not representative is discussed in the following section.

125 *b. Revealing the hysteresis*

126 The snow season usually starts at the beginning of October in the Upper Durance wa-
127 tershed and ends at the beginning of June as illustrated for catchment 3 in Figure 2a. More
128 than 80% of the catchment area is covered with snow for more than 5 months. From these
129 SCF time series, rates of SCF ($\frac{\Delta SCF}{\Delta t}$) were calculated and are displayed in Figure 2b. This
130 graph reveals clear differences in snow-cover dynamics between accumulation and ablation
131 events. The mean accumulation rate is 1.7 higher than the mean ablation rate which means
132 that the SCF increases faster than it decreases. This difference of variation rate strongly
133 suggests the existence of a hysteresis in the SCD as described by Luce et al. (1999).

134 Figure 3 shows, using snow depth measurements, a hysteresis in the SCD of catchment
135 3. This hysteresis was also observed in catchments 1 and 6 but not in the other elementary
136 catchments. This is likely because the point data in these catchments were not representative
137 of the mean snow depth as explained in Section 2a.

138 As suggested above, the hysteresis exists because the variables in the SCD, snow depths
139 and SCFs, are aggregated over the catchment and their values can represent different internal
140 states of the aggregated snowpack of the catchment. For example, if we consider a mean
141 snow depth of 40 cm, the SCF could be equal to 100% or to 40%. Reciprocally, if we
142 consider an SCF equal to 60%, the mean snow depth could be equal to 5 cm or 60 cm. In
143 addition, the configuration of the snowpack is not random in time. Figure 3 shows that
144 from October to December, the snow-cover extent of the catchment increases quickly with
145 a small amount of snow. Then the SCF remains constant along the horizontal asymptote of
146 full snow-coverage from December to February while snow depth increases to its maximum
147 value. Eventually, from March to June, a gradual reduction of the SCF occurs as the mean
148 snow depth decreases. This time pattern is due to the differences between the two processes
149 of accumulation and ablation. During accumulation, snowfall tends to spread uniformly
150 all over the catchment. By contrast, melting occurs in preferential locations. Snow stays
151 longer at high elevations, over north-facing slopes and in small hollows created by terrain

152 heterogeneities. Vegetation and wind-blown effect can also influence ablation of the snowpack
153 (Gray and Male 1981; Lundberg et al. 1998; Essery and Pomeroy 2004). As a result, the high
154 variability of topography and vegetation in each catchment (Table 1) explains the hysteresis
155 illustrated in Figure 3.

156 Consequently, the knowledge of a single characteristic of the aggregated snowpack, either
157 SWE or SCF, is not sufficient to describe its spatial setting. The subgrid variability of the
158 catchment must be accurately defined to predict the future development of the snowpack
159 which can be achieved by i) using a finer discretization (Lafaysse 2011), or ii) using a sub-
160 grid probability function, or iii) accounting for the history of the snowpack by means of a
161 hysteresis parameterization (Mielke and Roubícek 2003). In the latter case, lack of spatial
162 information is thus compensated by historical information.

163 Although the hysteresis could not be observed in all elementary catchments, differences
164 between SCF accumulation and ablation rates are confirmed for all of them (Figure 4).
165 Whereas ablation SCF rates are gathered close to zero, accumulation SCF rates are spread
166 over a larger range of values, and the mean accumulation rate is 1.65 times higher than the
167 ablation rate. From this result and those found in catchments 1, 3 and 6, we assume that
168 this hysteresis exists in every elementary catchment of the Upper Durance watershed.

169 **3. Modeling concepts**

170 *a. General principles*

171 CLSM stands for Catchment Land Surface Model (Koster et al. 2000; Ducharne et al.
172 2000). As a land surface model (LSM), it is designed to simulate the diurnal cycle of land
173 surface water and energy fluxes as a function of near-surface meteorology (precipitation,
174 short and long-wave incident radiation, surface pressure, air temperature and humidity at 2
175 m, and wind speed at 10 m) ; it can be either be coupled to a GCM or used off-line as in this
176 present study. A characteristic of this LSM is to relate sub-grid soil moisture heterogeneities

177 with topography using TOPMODEL concepts (Beven and Kirkby 1979). The topographic
178 index is a soil moisture indicator and is formulated as follows:

$$x = \ln(a/\tan\beta), \quad (1)$$

179 where a is the upslope contributing area per unit contour length and $\tan\beta$ is the local
180 topographic slope. High values of the topographic index denote low land easily liable to
181 saturation whereas low values result from small drainage areas and steep slopes, characteristic
182 of mountain ridges.

183 Hydrological catchments are used as the fundamental land surface element and horizontal
184 soil moisture variability within each catchment is described on the basis of the topographic
185 index distribution. This resulting distribution of soil moisture allows partitioning into three
186 areal fractions with distinct hydrological functioning: stressed, intermediate and saturated
187 (e.g., no evapotranspiration takes place from the stressed fraction). These fractions vary
188 in time as a result of the catchment water budget, with an increased stressed fraction in
189 dry periods and an increased saturated fraction in wet periods. Fluxes, such as evapotran-
190 spiration or runoff, are described using classic soil-vegetation-atmosphere transfer (SVAT)
191 formulations, mostly taken from the Mosaic LSM (Koster and Suarez 1996).

192 *b. Description of the sub-grid variability of vegetation*

193 Eight classes of vegetation are defined in the CLSM and proportions of each were ex-
194 tracted from ECOCLIMAP, a global database of land surface parameters at 1 km resolu-
195 tion(Masson et al. 2003). The vegetation classes are summarized into three main types of
196 land cover in Table 1, which shows that different types of vegetation coexist in similar pro-
197 portions. They have very distinct properties (LAI, albedo, etc.) and are likely to play a
198 key role in the subgrid variability of the snow-cover extent illustrated in Figure 3. We thus
199 decided to allow a mosaic of vegetation types, in contrast to the latest studies (Koster et al.
200 2000; Ducharne et al. 2000; Stieglitz et al. 2001a; Déry et al. 2004; Gascoin et al. 2009b),

201 which assumed that the catchment was uniformly covered with the dominant vegetation.
 202 The resulting vegetation 'tiles' share the same soil moisture variables, but they have inde-
 203 pendent energy budgets and the snow model is applied to each vegetation tile. We refer to
 204 this configuration of the CLSM as 'multi-tile' in the following sections.

205 *c. Initial snow-cover parameterization*

206 The multilayer, physically based snow scheme included in the CLSM (Lynch-Stieglitz
 207 1994) is of intermediate complexity according to Boone and Etchevers (2001) classification
 208 of snow schemes and has shown good performance in different studies (Stieglitz et al. 2001b;
 209 Gascoïn et al. 2009b; Koster et al. 2010). The snow model vertically discretizes the snowpack
 210 into 3 layers, each of them is characterized by its heat content, snow water equivalent (SWE)
 211 and snow depth (Lynch-Stieglitz 1994; Stieglitz et al. 2001a; Déry et al. 2004). As detailed
 212 in Lynch-Stieglitz (1994), these variables vary in time by means of three processes:

- 213 • heat transfer between the atmosphere and the snowpack surface layer (sublimation,
 214 condensation or sensible heat flux) and between each layer (thermal diffusion);
- 215 • mass transfer between the atmosphere and the snowpack surface layer (precipitation),
 216 and between the layers (melt water); and
- 217 • snow compaction in each layer.

218 A threshold of SWE, W_{min} of $13\text{kg}\cdot\text{m}^{-2}$, was set to ensure a smooth transition between
 219 snow-free and snow-covered conditions. When the SWE is less than W_{min} , the SCF of the
 220 catchment, F , is defined as follows:

$$F = \begin{cases} \frac{W}{W_{min}} & \text{if } W < W_{min} \\ 1 & \text{if } W \geq W_{min} \end{cases} \quad (2)$$

221 where W is the snow water equivalent ($\text{kg}\cdot\text{m}^{-2}$) of the catchment. Figure 5a displays the
 222 initial SCD. Once the SWE reaches W_{\min} and stays above this value, the SCF is equal to 1
 223 and the snowpack grows vertically rather than horizontally. The snow cover is assumed to
 224 remain spatially uniform across the catchment, with depth being spatially constant.

225 *d. New snow-cover depletion curve with hysteresis*

226 Aspect and slope also play a significant role during the melt (Liston 2004), and accounting
 227 for the sub-grid variability of vegetation may not be enough to reproduce the hysteresis
 228 demonstrated in section 2. Therefore, we decided to introduce a hysteresis in the initial
 229 SCD using a new parameter, W_{melt} . During accumulation, the SCF quickly increases with
 230 initial snowfall and the relationship between the SCF and SWE is the initial one (Equation
 231 2). During ablation, the SCF stays at full cover until SWE drops lower than W_{melt} , at which
 232 point there is a more gradual reduction in SCF as in Figure 3. The SCF is then calculated
 233 as follows:

$$F = \begin{cases} \min\left(\frac{W}{W_{\min}}, 1\right) & \text{if } dW \geq 0 \\ \min\left(\frac{W}{W_{\text{melt}}}, 1\right) & \text{if } dW < 0 \end{cases} \quad (3)$$

234 where dW is the variation of SWE between two time steps and W_{melt} is the new pa-
 235 rameter characterizing the ablation part of the curve. It should depend on terrain aspect
 236 and topography, thus being catchment-specific, but it was defined empirically in this study
 237 (see Section 5d). Because of melt events occurring when accumulation prevails, conditions
 238 related to the variation in SWE were added to prevent a substantial decrease of the SCF
 239 when melt events are small. Note also that the melting rate is assumed to be uniform in
 240 each catchment unit. This is not a limitation because the spatial distribution of the melting
 241 rate can be refined by decreasing the catchment size.

4. Application to the Durance watershed

a. Topographic indices and surface parameters

The 25-m DEM was also used to calculate the topographic indices. Their minimum values in the Upper Durance River region are lower than in catchments located downstream, indicating that the slopes are steeper. This is in good agreement with Table 1 showing a high degree of topographic variability within each catchment in this region.

Vegetation parameters (LAI, albedo, roughness length, soil depth) were extracted from the ECOCLIMAP database. In addition to forests, grassland and bare soil, a small proportion of glacier remains in the Upper Durance watershed according to ECOCLIMAP (2.5%), but is not taken into account in the CLSM. From the fractions of sand and clay provided by ECOCLIMAP, soil texture was defined using the USDA triangle from which soil parameters, such as porosity, hydraulic conductivity, matric potential at saturation and wilting point, were deduced following the values of Cosby et al. (1984).

b. Meteorological data

SAFRAN, a mesoscale atmospheric reanalysis over France (Quintana-Seguí et al. 2008; Vidal et al. 2009), provides the seven meteorological forcings needed by the CLSM at an hourly time step and on a 8-km grid : rainfall (Rain) and snowfall (Snow), incoming long wave and shortwave radiation ($LW\downarrow$ and $SW\downarrow$), air temperature (T) and humidity(Q) at 2 m and wind speed(V) at 10 m. However, SAFRAN underestimates precipitation, especially snowfall (Lafaysse 2011). This could be explained by the scarcity of meteorological stations at high altitudes and a poor capture of snowflakes by rain gauges. SPAZM is another meteorological reanalysis recently elaborated for the French mountains (Gottardi 2009). This new analysis uses more ground observations and a statistical approach that accounts for the orographic effect on precipitation based on weather patterns. Precipitation is 27% higher in SPAZM than in SAFRAN, and the difference in precipitation can reach 70% in the Massif des Ecrins

267 (north-west of the watershed) where snowfall is dominant. In addition to being more realistic,
 268 this dataset has a finer resolution than SAFRAN as it provides information on a 1-km grid.
 269 However, only daily mean temperatures and precipitation are given.

270 A hybridization of SAFRAN and SPAZM was performed to take advantage of the two
 271 datasets whose characteristics are summarized in Table 2. It consists of correcting and
 272 downscaling SAFRAN data based on SPAZM monthly mean temperatures and precipitation
 273 totals, using a method similar to that of Sheffield et al. (2006). Biases of precipitation in
 274 SAFRAN were first removed by scaling the hourly values so that their monthly totals match
 275 those of SPAZM:

$$276 \quad P(x_{sp}, y_{sp}, h) = P_{SAF}(x_{sa}, y_{sa}, h) * \frac{\sum P_{SPAZM}(x_{sp}, y_{sp})}{\sum P_{SAF}(x_{sa}, y_{sa})} \quad (4)$$

277 where x_{sp}, y_{sp} are the 1-km 'SPAZM' grid cell coordinates; x_{sa}, y_{sa} , are the 8-km 'SAFRAN'
 278 grid cell coordinates, h , is the hour index and $\sum P_{SPAZM}$ and $\sum P_{SAF}$ are the monthly
 279 SPAZM and SAFRAN precipitation totals.

280 The temperature data from SAFRAN were adjusted to match the SPAZM monthly val-
 281 ues by shifting the SAFRAN hourly values by the difference between the SPAZM and the
 282 SAFRAN monthly means in accordance with:

$$T(x_{sp}, y_{sp}, h) = T_{SAF}(x_{sa}, y_{sa}, h) + \left(\overline{T_{SPAZM}(x_{sp}, y_{sp})} - \overline{T_{SAF}(x_{sa}, y_{sa})} \right) \quad (5)$$

283 with $\overline{T_{SPAZM}}$ and $\overline{T_{SAF}}$ being the monthly air temperature means.

284 To partition precipitation between rainfall and snowfall, a threshold air temperature was
 285 set to 1° C. This temperature is derived from Hingray et al. (2010), who defined an empirical
 286 relationship between the precipitation phase and the temperature using 17 stations located
 287 above 1000 m in the Swiss Alps. At this stage, temperature, snowfall and rainfall were
 288 obtained on a 1-km grid and the mean elevation of the grid cell was extracted using the
 289 25-m DEM. From these variables, assuming that relative humidity is held constant between
 290 the 'SAFRAN' and the 'SPAZM' grid cells to avoid the possibility of air supersaturation, we

291 corrected specific humidity and incoming long wave radiation using the methods of Cosgrove
292 et al. (2003) (equations listed in Appendix 7). The values of wind and incoming shortwave
293 radiation on a 'SPAZM' grid cell were kept equal to the values of the 'SAFRAN' grid cell to
294 which they belong.

295 The resulting reanalysis, an hourly dataset of seven meteorological variables on a 1-km
296 grid, is called DuO (Durance MétéO). Its characteristics are listed in Table 2. We verified
297 that the daily distributions of precipitation and temperature between DuO and SPAZM as
298 well as the ratio snowfall/rainfall between DuO and SAFRAN are consistent. Using DuO
299 meteorological forcing improved the simulations of the water budget, as it was shown in
300 previous studies using other hybridized datasets (Ngo-Duc et al. 2005; Dirmeyer 2005; Guo
301 et al. 2006; Weedon et al. 2011), .

302 According to the DuO dataset, the Upper Durance watershed receives approximately
303 1300 mm of precipitation per year, of which 48% is snowfall, and its mean temperature is
304 about 4.5 °C, with a range of -5 °C to 15 °C in a year. Temperatures and precipitation are
305 marked by an orographic effect, with temperatures being lower and precipitation greater in
306 catchments at higher elevations. In addition to this orographic effect, precipitation is also
307 influenced by the westerly general circulation over France; catchments located in the western
308 part of the Upper Durance River watershed receive more precipitation than those located in
309 the eastern part. Note that snowfall varies greatly from year to year: as an example, annual
310 snowfall ranges from 250 to 850 mm/yr in catchment 3.

311 *c. Two independent validation datasets*

312 Simulated SCFs were validated using the observed SCFs derived from the MODIS im-
313 ages as described in Section 2a and observed daily discharges provided by Electricité de
314 France (EDF) were used to validate runoff simulations. There are six gauging stations in
315 the Upper Durance river watershed (Figure 1, Table 1). Discharges at the watershed outlet,
316 depicted in red in Figure 1, were reconstructed i.e., the dam's influences were subtracted

317 from observed discharges to reconstruct the discharges that would be observed without hu-
318 man disturbances. Because no routing procedure is included in the CLSM, we averaged the
319 runoff of the upstream catchments over 10 days (a longer period than the residence time) to
320 compare simulations with observations. Then the spatially weighted-average of runoff was
321 calculated and the mean observed discharge over 10-days converted into runoff.

322 Discharge observations show a nival regime with highly seasonal flows. The main peak
323 flows occur in spring from April to June, with two low flow periods, one in winter, during
324 snow accumulation and another in summer, when precipitation is low.

325 5. Results

326 *a. Modeling strategy*

327 A set of numerical experiments (summarized in Table 3) were conducted with the CLSM
328 to understand the impacts of different parameterizations on the water and energy budgets.
329 Two types of simulations were performed: the first type, called REF, with the initial con-
330 figuration of the snow model, i.e, $W_{\text{melt}} = W_{\text{min}}$, and the second, called HYST, with the
331 hysteresis in the SCF parameterization. W_{melt} should depend on the terrain heterogeneities
332 but was calibrated here by comparison with discharge observations to obtain the best per-
333 formances using the relative bias and the Nash-Sutcliffe coefficient.

334 The influence of vegetation on snowpack dynamics was tested for both the REF and
335 HYST versions. The catchments are either partitioned into different tiles of vegetation, in
336 simulations referred as 'multi-tile', or covered with 100% of the same type of land cover, in
337 simulations referred as 'single-tile' (Table 3). REF200, REF400 and REF600 simulations
338 were performed to test the sensitivity of the CLSM responses to W_{min} .

339 Three hydrodynamic parameters related to the TOPMODEL concepts used in the CLSM
340 were calibrated for the HYST simulation following Gascoin et al. (2009a): K_0 , the saturated
341 hydraulic conductivity at the soil surface; ν , characterizing the decay of the saturated hy-

342 draulic conductivity with depth; and, D , the depth to bedrock. They were selected to give
343 the best performances in terms of runoff, low bias and high Nash-Sutcliffe coefficient for
344 simulation HYST. All the simulations mentioned above used the same set of hydrodynamic
345 parameters. After initializing the CLSM for three years, all simulations were run for 30 years
346 between August 1980 and July 2009.

347 *b. Initial snow-cover parameterization*

348 The REF simulation allows the coexistence of three types of land cover, forests, grassland
349 and bare soil (cf. Table 1), within an elementary catchment via the 'mosaic' approach
350 adopted in this study (Section 3b). Figure 6 shows that the duration of snow cover and the
351 maximum SWE strongly depends on the land cover. The snowpack dynamics will indeed
352 depend on vegetation via two parameters, albedo and vegetation roughness length. (i) The
353 albedo of the snow-cover fraction (SCF) is reduced by a snow masking depth depending on
354 the vegetation type (Hansen et al. 1983). (ii) Evaporation and sublimation are enhanced
355 by turbulent fluxes (Brutsaert 2005) so that more sublimation is produced over vegetation
356 with high roughness length (i.e., small aerodynamic resistance) than over vegetation with
357 low roughness length. Because of these two parameters, the development and duration of
358 the snowpack are different from tile to tile with identical meteorological forcings.

359 The shape of the SCD initially implemented in the snow-model (Figure 5a) is recogniz-
360 able in the single-tile simulations ($\text{REF}_{\text{forest}}$, $\text{REF}_{\text{grass}}$ and REF_{bs} , Figure 6b, Figure 6c and
361 Figure 6d respectively), but it is not recognizable in the REF simulation using a multi-tile
362 configuration (Figure 6). The combination of different vegetation tiles, each influencing the
363 snowpack dynamics differently, leads to a vegetation-driven hysteresis in the SCD at the
364 catchment scale (Figure 6a). Nevertheless, the ablation part of this curve is mostly parallel
365 to the accumulation part, while the analysis of MODIS data (Figures 2, 3 and 4) suggests
366 that the slopes of the two branches should differ more.

367 In terms of runoff, the REF simulation gives a good runoff volume with relative biases

368 ranging from -5% to 8% for all catchments, but shows a peak discharge that starts too early
369 and is sharper compared to the observed runoff as shown in red in Figure 7a. The simulated
370 snowpack seems to melt faster than the real one.

371 Nevertheless, SCFs from the REF simulation show good consistency with MODIS ob-
372 servations as illustrated in Figure 7b. The coefficient of correlation ($r = 0.94$) calculated
373 over 2000-2009 between the simulated and observed maximum snow extent over eight days
374 confirms this result. Figure 7b also highlights a too sudden decrease in simulated SCFs when
375 the snow melts, uncovering the catchment two to three weeks earlier than the more gradual
376 decrease of observed SCFs. This early decrease in simulated SCFs is in good agreement
377 with the lag previously noticed between observed and simulated runoff and supports the
378 assumption that melting processes are not well represented in the CLSM.

379 *c. Sensitivity to W_{min}*

380 To assess the influence of the SCF parameterization on snowpack dynamics and on the
381 water budget, we tested the sensitivity of the runoff and the SCF simulation to W_{min} by
382 increasing this parameter from 13 to 200, 400 and 600 $\text{kg}\cdot\text{m}^{-2}$. W_{min} was recently increased
383 by Reichle et al. (2011) to 26 $\text{kg}\cdot\text{m}^{-2}$ to improve the stability of the surface flux calculation
384 when snow is present. Increasing W_{min} implies that more snow is needed on the catchment
385 to obtain a full snow coverage. Figure 7a shows that increasing W_{min} delays and attenuates
386 the peak discharge. The REF400 simulation, especially, is well synchronized with the ob-
387 servations and Nash-Sutcliffe coefficients increase from 0.06 for the REF simulation to 0.47
388 for the REF400 simulation. The bias between observations and these two simulations, REF
389 and REF400, tend to slightly decrease, but no significant change is found in the volume.

390 Despite these improvements regarding the runoff simulation, simulations of SCFs with
391 high W_{min} are significantly deteriorated and are too small compared to the MODIS obser-
392 vations (Figure 7b). As an example, SCFs from simulation REF600 with the highest W_{min}
393 never reach 100% whereas observed SCFs do indicate full or almost full snow coverage of the

394 catchment in winter. Correlation coefficients decrease from 0.88 when $W_{\min} = 13$ to 0.47
395 when $W_{\min} = 600$. Yet, snow stays longer in the catchment when increasing W_{\min} , which is
396 consistent with the observations. Simulation REF400, in which runoff is well phased com-
397 pared to the observed peak discharge, captures the melting part of the SCFs evolution fairly
398 well.

399 These results show that increasing W_{\min} does have an effect on the snow-melt process
400 and improves the runoff simulation, but this is at the expense of the SCFs simulation that
401 underestimates the observations.

402 *d. Introducing the hysteresis in the SCF parameterization*

403 The melt is not well simulated with the initial snow-cover parameterization; this is likely
404 because other factors than vegetation, such as slopes and aspect, influence the evolution of
405 the snow-cover extent. Implementing the hysteresis in the SCD allows these factors to be
406 taken into account. Table 1 shows the different values of W_{melt} calibrated for each catchment.
407 As expected, the upstream catchments most influenced by snow have higher W_{melt} . Figure
408 8a shows an improvement in the peak discharge timing and rate between REF and HYST.
409 The peak discharge of the HYST simulation starts later, lasts longer and is thus closer to
410 the observed peak discharge.

411 Considering all gauged catchments, Figure 9 shows how closely the runoff and SCF
412 simulations REF and HYST match their respective observations (discharge at the 6 gauging
413 stations and MODIS images). The correlation coefficients for runoff simulations increase
414 from REF to HYST without deteriorating the normalized standard deviation, reflecting the
415 amplitude of the time series. Therefore, Figure 9 confirms that the dynamics of melt is getting
416 better for all gauged catchments of the Upper Durance. Besides, the bias remains within a
417 satisfactory range of values although it slightly increases from REF to HYST. Concerning the
418 SCFs simulations, no significant difference between simulations REF and HYST is shown,
419 neither in terms of dynamics (empty and full triangles are more or less superimposed) nor

420 in terms of volume (similar bias). As a consequence, the new SCF parameterization leads
421 to a more realistic runoff simulation in all the studied catchments without a significant
422 deterioration of the SCF simulation.

423 In general, the introduction of the hysteresis maintains more snow over the catchment
424 during a longer period. The maximum SWE over the catchment is on average 25% more
425 important in the HYST simulation than in the REF simulation, and the snow-covered period
426 lasts on average 10 days longer (Table 4). At the end of spring, the SCFs are sometimes
427 overestimated by the HYST simulation, as illustrated in Figure 8b for 2003-2004, leading to
428 a slight increase of the RMSE from REF to HYST.

429 Yet on average, the coefficients of correlation remain around 0.9 for all catchments and
430 become variable when computed over individual years (Table 4). MODIS observations are
431 better reproduced by the HYST simulation than by the REF simulation when the amount of
432 snowfall is low as in 2004-2005. The annual snowfall is 35% smaller than the mean amount
433 over 2000-2010; 40% of the snowfall occurs between October and January, then almost no
434 snowfall from January to March, and an important snowfall event in April accounting for
435 46% of the total amount of snowfall. The low snowfall between January and March can be
436 seen in Figure 8b in the observations and in both simulations. This period of low snowfall
437 is better simulated by HYST with an SCF of 70% maintained over the catchment, whereas
438 REF strongly underestimates the snow cover extent. The high frequency of SCF values
439 of 70% in the two simulations, REF and HYST, especially at the end of the snow season
440 in 2003-2004 and in 2005-2006, is due to the faster disappearance of snow over forests as
441 explained in Section 5b.

442 The hysteresis implemented in the SCD modifies the evolution of the SCF and, thus, the
443 energy budget. The increased duration of snow cover leads to a decrease of net radiation
444 (-8%)(more upward radiation), thus reducing the energy available for the turbulent fluxes.
445 As a result, the mean surface temperature decreases by 0.8 °C. The increased duration of
446 snow cover also leads to decreased transpiration and evaporation from bare soil (-2% and

447 -9%, respectively) by preventing transpiration from the vegetation and evaporation from
448 bare soil. The increase of the mean SWE is caused by the increased duration of the snow
449 cover and a slight decrease in sublimation (-2%). The decrease of these components of
450 evapotranspiration leads to an increase in runoff (Figure 9). Both energy and water budgets
451 are therefore impacted by the new SCF parameterization.

452 6. Discussion

453 To assess the impacts of the SCF parameterization with hysteresis on each type of land
454 cover and their contribution to the changes noted at the catchment scale, we performed
455 three other simulations of type HYST accounting for only one type of land cover (Table
456 3) as we did for type REF in the previous Section. Figure 10 shows that changes between
457 REF and HYST over bare soil and grassland are in the same direction and contribute the
458 most to the changes of the multi-tile simulation HYST. In contrast, the changes over forests
459 are very small and the introduction of the hysteresis does not really impact the evolution
460 of the snowpack. This could be explained by the fact that an important difference between
461 the three types of land cover is the repartition of snowpack ablation between melt and
462 sublimation. Over forested areas (mainly needleleaf), sublimation losses are important and
463 account on average for 250 mm/year in the Upper Durance watershed, i.e., 45% of the snow
464 cover ablation in good agreement with Lundberg et al. (1998) and Pomeroy et al. (1998).
465 In contrast, sublimation losses account only for 4% and 7%, respectively, of the snowpack
466 ablation over bare soil and grassland.

467 W_{melt} was introduced to strengthen the hysteresis of the SCD at the catchment scale and
468 is likely to account for the influence of topography and aspect on the melting process. It
469 is therefore normal that the impacts of the SCF parameterization with hysteresis are more
470 important in tiles where melt is the dominant ablation process. Moreover, Ellis et al. (2013)
471 showed that the effect of aspect (north- or south-facing) on melt is less important in forests

472 than in open landscapes such as bare soil or grassland. This is again consistent with the
473 fact that forested areas are not impacted by the introduction of the hysteresis in the SCF
474 parameterization. In Section 5d, we demonstrated that the parameter W_{melt} does change the
475 dynamics of the melt, but does not significantly change the sublimation losses (only -2%),
476 and thus maintains the same repartition between melt and sublimation in terms of volume.

477 The multi-tile configuration and the parameter W_{melt} represent two types of sub-grid
478 variability that do not influence the snowpack in the same way. The multi-tile configuration
479 is mainly related to the sub-grid sublimation variability, a process that occurs throughout
480 the snow-season, especially at its beginning (Hood et al. 1999), whereas the parameter W_{melt}
481 is related to the melt occurring mainly at the end of the snow season. Note that sublimation
482 contributes to 18% of the snow-cover ablation using the multi-tile simulation HYST and this
483 is consistent with the values reported for mid-latitude Alpine catchments, ranging between
484 15% to 20% (Kattelmann and Elder 1991; Marks et al. 1992; Hood et al. 1999).

485 7. Conclusion

486 In this article we first highlighted the differences in dynamics between accumulation and
487 depletion of the snow cover in the Alps using MODIS snow-cover extent images. Indeed,
488 we demonstrated that the SCF increases faster than it decreases. The use of snow-depth
489 measurements allowed us to confirm that the difference between SCF accumulation and
490 ablation rates is due to the existence of a hysteresis in the SCD at the catchment scale as
491 Swenson and Lawrence (2012) and Luce et al. (1999) highlighted in other environments.
492 We then applied the CLSM in the Upper Durance watershed. Although, the initial snow-
493 cover parameterization of the CLSM captures the overall evolution of the SCFs fairly well,
494 it cannot reproduce the melting period. The catchment is uncovered few weeks earlier than
495 in the MODIS observations and the spring thaw is not well simulated.

496 We demonstrated the efficiency of introducing a hysteresis in the SCD to correctly simu-

497 late melting events and the dynamics of snow-cover extent. This led to a great improvement
498 in reproducing the timing and shape of the spring thaw. It also increased the duration of
499 the snow cover in agreement with the MODIS observations and improved the simulation of
500 the SCF evolution in years with a small amount of snowfall. This is important given that
501 less snow is expected in these regions because of climate change.

502 However we noted an overestimation of the simulated SCFs compared to MODIS images
503 at the end of spring. This may be related to a shortcoming of the model in which the snow
504 depth is assumed to be uniform. Hence, when snow falls on a heterogeneous snow cover (SCF
505 < 1), the resulting SWE is uniformly redistributed, leading to stronger insulation, thus lower
506 surface temperatures during snow melt, than if the memory of heterogeneous snow depths was
507 kept. It is noteworthy that the resulting snow depth heterogeneities can be enhanced by the
508 so-called wind-blown effect which leads to redistributing snow and increasing sublimation,
509 especially at high altitudes where wind speed is high (Liston 2004; Strasser et al. 2008;
510 Gascoin et al. 2012). Two strategies could be explored to solve this problem, either by using
511 the CLSM at a much higher resolution, or by introducing a statistical distribution of snow
512 depth within the elementary catchments following (Liston 2004). Part of the discrepancies
513 between the model and the observations may also be due to the lack of explicit representation
514 of the snow/vegetation interactions in the CLSM snow scheme, especially in forested zones
515 (Rutter et al. 2009).

516 Anyway, the new snow cover parameterization introduced in this paper allowed us to
517 get a satisfactory simulation of both runoff and snow-cover extent without increasing the
518 computational load. The parameter W_{melt} was calibrated for simplicity but it should depend
519 on morphological features of the catchment such as mean elevation, elevation range, terrain
520 roughness, or hillslope orientation. A generic application of the parameterization would thus
521 require to find a relationship between these morphological parameters and W_{melt} which might
522 benefit from the use of hydrological catchment as elementary land surface units in the CLSM.
523 The combination of such a relationship with the physically-based snow description and the

524 multi-tile configuration of the CLSM would then offer an approach that is flexible enough
525 to account for various impacts of global change on snow dynamics and water resources in
526 Alpine environments, from climate change to land cover change.

527 *Acknowledgments.*

528 This work has been carried out in the framework of the project R²D²-2050 supported by
529 the programme Gestion et Impact du Changement Climatique of the Ministère de l'Écologie,
530 du Développement Durable et de l'Énergie. Claire Magand was supported by a grant from
531 l'Agence de l'Eau Rhône Méditerranée Corse. Simon Gascoin was supported by Fondecyt
532 Chile (Grant 11090445). The authors are grateful for the meteorological data from the
533 SAFRAN database provided by Météo-France and from the SPAZM database provided by
534 Frederic Gottardi of Électricité de France. We also wish to thank Thibault Mathevet of
535 Électricité de France for providing us naturalized flows.

APPENDIX

536

537

538 **Meteorological dataset construction : equations form**

539 *a. Air pressure*

540 Surface air pressure is determined from elevation using :

541

$$P(z) = P_0 \exp\left(-\frac{gM_a}{RT}z\right) \quad (\text{A1})$$

542 with P_0 , being the surface air pressure at sea level (Pa), g the gravitational constant
543 (m.s⁻²), M_a , the air molar mass (kg.mol⁻¹), R the gas constant (J.K⁻¹.mol⁻¹), and T the
544 air temperature (K). The temperature is considered equal to 15 °C (Allen et al. 1998).

545 *b. Air specific humidity*

546 It is important to modify specific humidity when changing air temperature to avoid the
547 possibility of super saturation. Like Cosgrove et al. (2003), we assume that the relative
548 humidity is held constant between the SAFRAN and the SPAZM grid cells.

549

$$RH = \left(\frac{q(z_{sp}, t)}{q_{sat}(z_{sp}, t)}\right) * 100 = \left(\frac{q(z_{sa}, t)}{q_{sat}(z_{sa}, t)}\right) * 100, \quad (\text{A2})$$

550 with z_{sa} , being the elevation of the SAFRAN grid cell and z_{sp} the elevation of the SPAZM
551 grid cell. The specific humidity in SPAZM cell is calculated from this equation A2 and from
552 the value given by SAFRAN.

553 The specific humidity at saturation, q_{sat} , is then calculated as follows :

$$q_{sat} = \frac{0.622e_s}{P - 0.378e_s}, \quad (\text{A3})$$

554 where e_s is the vapor pressure (hPa).

555 There are many empirical equations to determine vapor pressure; the one we use comes
 556 from the reference report about evapotranspiration written by Allen et al. (1998).

557

$$e_s = 6.108; \exp \left[\frac{17.27(T - 273.15)}{(T - 273.15) + 237.3} \right] \quad (\text{A4})$$

558 *c. Incident longwave radiation*

559 Incident longwave radiation $IR \downarrow$ is described by the Stefan-Boltzmann law. Brutsaert
 560 (1982) simplifies this equation as follows :

561

$$IR \downarrow = \epsilon_{ac} \sigma T_a^4, \quad (\text{A5})$$

562 where

563 i. σ , is the Stefan-Boltzmann constant, equal to $5.6704 \cdot 10^{-8} W \cdot m^{-2} \cdot K^{-4}$,

564 ii. T_a , is the air temperature (K), and

565 iii. ϵ_{ac} , is atmospheric emissivity under clear skies, estimated using:

566

$$\epsilon_{ac} = 1.24 \left(\frac{e_a}{T_a} \right)^{1/7} \quad (\text{A6})$$

567 In this equation, e_a is the vapor pressure (mb) equal to :

568

$$e_a = \frac{qP}{\zeta}, \quad (\text{A7})$$

569 with q being the specific air humidity, P the surface air pressure, and ζ the ratio between
 570 the water and air molar masses. We assumed that the variation of emissivity with elevation
 571 is similar whether the sky is clear or clouded, where:

$$\frac{\epsilon_{ac}(z_{sp})}{\epsilon_{ac}(z_{sa})} = \frac{\epsilon_n(z_{sp})}{\epsilon_n(z_{sa})} \quad (\text{A8})$$

572 ϵ_n is the emissivity accounting for cloudiness.

573 By combining the equations listed above, the incident longwave radiation is calculated ac-
574 cording to the following equation.

575

$$IR \downarrow (z_{sp}, t) = \left[\frac{IR \downarrow (z_{sa}, t)}{\sigma T(z_{sa}, t)^4} \left(\frac{q(z_{sp}, t)P(z_{sp})T(z_{sa}, t)}{q(z_{sa}, t)P(z_{sa})T(z_{sp}, t)} \right)^{1/7} \right] \sigma T(z_{sp}, t)^4. \quad (\text{A9})$$

576

577

REFERENCES

- 580 Allen, R., L. Pereira, D. Raes, M. Smith, et al., 1998: Crop evapotranspiration-Guidelines for
581 computing crop water requirements-FAO Irrigation and drainage paper 56. *FAO, Rome*,
582 **300**, 6541.
- 583 Beven, K. and M. Kirkby, 1979: A physically based, variable contributing area model of
584 basin hydrology/un modèle à base physique de zone d'appel variable de l'hydrologie du
585 bassin versant. *Hydrological Sciences Journal*, **24 (1)**, 43–69.
- 586 Boone, A. and P. Etchevers, 2001: An intercomparison of three snow schemes of varying
587 complexity coupled to the same land surface model: Local-scale evaluation at an Alpine
588 site. *Journal of Hydrometeorology*, **2 (4)**, 374–394.
- 589 Brutsaert, W., 1982: *Evaporation into the atmosphere: Theory, history, and applications*,
590 Vol. 1. Springer.
- 591 Brutsaert, W., 2005: *Hydrology: an introduction*. Cambridge Univ Pr.
- 592 Cosby, B., G. Hornberger, R. Clapp, and T. Ginn, 1984: A statistical exploration of the
593 relationships of soil moisture characteristics to the physical properties of soils. *Water*
594 *Resour. Res*, **20 (6)**, 682–690.
- 595 Cosgrove, B., et al., 2003: Real-time and retrospective forcing in the North American Land
596 Data Assimilation System (NLDAS) project. *J. Geophys. Res*, **108 (D22)**, 8842.
- 597 Déry, S., W. Crow, M. Stieglitz, and E. Wood, 2004: Modeling Snow-Cover Heterogeneity
598 over Complex Arctic Terrain for Regional and Global Climate Models. *Journal of Hy-*
599 *drometeorology*, **5 (1)**, 33–48.

600 Dirmeyer, P., 2005: *The second Global Soil Wetness Project (GSWP-2): Multi-model anal-*
601 *ysis and implications for our perception of the land surface*, Vol. 185. Center for Ocean-
602 Land-Atmosphere Studies.

603 Douville, H., J. Royer, and J. Mahfouf, 1995: A new snow parameterization for the meteo-
604 france climate model. *Climate Dynamics*, **12** (1), 21–35.

605 Ducharne, A., R. Koster, M. Suarez, M. Stieglitz, and P. Kumar, 2000: A catchment-based
606 approach to modeling land surface processes in a general circulation model: 2. parameter
607 estimation and model demonstration. *J. Geophys. Res.*, **105** (24), 823–24.

608 Dutra, E., G. Balsamo, P. Viterbo, P. M. Miranda, A. Beljaars, C. Schär, and K. Elder,
609 2010: An improved snow scheme for the ECMWF land surface model: description and
610 offline validation. *Journal of Hydrometeorology*, **11** (4), 899–916.

611 Ellis, C., J. Pomeroy, and T. Link, 2013: Modeling increases in snowmelt yield and desyn-
612 chronization resulting from forest gap-thinning treatments in a northern mountain head-
613 water basin. *Water Resources Research*.

614 Essery, R. and J. Pomeroy, 2004: Implications of spatial distributions of snow mass and melt
615 rate for snow-cover depletion: theoretical considerations. *Annals of Glaciology*, **38** (1),
616 261–265.

617 Gascoin, S., A. Ducharne, P. Ribstein, M. Carli, and F. Habets, 2009a: Adaptation of a
618 catchment-based land surface model to the hydrogeological setting of the Somme River
619 basin (France). *Journal of Hydrology*, **368** (1), 105–116.

620 Gascoin, S., A. Ducharne, P. Ribstein, Y. Lejeune, P. Wagnon, et al., 2009b: Dependence of
621 bare soil albedo on soil moisture on the moraine of the Zongo glacier (Bolivia): Implications
622 for land surface modeling. *Journal of Geophysical Research*, **114**, D19 102.

- 623 Gascoin, S., S. Lhermitte, C. Kinnard, K. Borstel, and G. E. Liston, 2012: Wind effects on
624 snow cover in pascua-lama, dry andes of chile. *Advances in Water Resources*.
- 625 Gottardi, F., 2009: Estimation statistique et réanalyse des précipitations en montagne. utili-
626 sation débauches par types de temps et assimilation de données d’enneigement. application
627 aux grands massifs montagneux français. Ph.D. thesis, Université Joseph Fourier, Greno-
628 ble. Institut National Polytechnique de Grenoble (INPG). LTHE.
- 629 Gottardi, F., C. Obled, J. Gailhard, and E. Paquet, 2012: Statistical reanalysis of precipita-
630 tion fields based on ground network data and weather patterns: Application over French
631 mountains. *Journal of Hydrology*, **432**, 154–167.
- 632 Gray, D. and D. Male, 1981: *Handbook of Snow: Principles, Processes*, Vol. 776.
- 633 Guo, Z., P. Dirmeyer, Z. Hu, X. Gao, and M. Zhao, 2006: Evaluation of the Second Global
634 Soil Wetness Project soil moisture simulations: 2. Sensitivity to external meteorological
635 forcing. *J. Geophys. Res*, **111**, D22S03.
- 636 Hansen, J., G. Russell, D. Rind, P. Stone, A. Lacis, S. Lebedeff, R. Ruedy, and L. Travis,
637 1983: Efficient three-dimensional global models for climate studies: Models I and II.
638 *Monthly Weather Review*, **111** (4), 609–662.
- 639 Hingray, B., B. Schaeffli, A. Mezghani, and Y. Hamdi, 2010: Signature-based model cali-
640 bration for hydrological prediction in mesoscale alpine catchments. *Hydrological Sciences*
641 *Journal–Journal des Sciences Hydrologiques*, **55** (6), 1002–1016.
- 642 Hood, E., M. Williams, and D. Cline, 1999: Sublimation from a seasonal snowpack at a
643 continental, mid-latitude alpine site. *Hydrological Processes*, **13** (1213), 1781–1797.
- 644 Kattelmann, R. and K. Elder, 1991: Hydrologic characteristics and water balance of an
645 alpine basin in the Sierra Nevada. *Water Resources Research*, **27** (7), 1553–1562.

- 646 Koster, R. and M. Suarez, 1996: Energy and water balance calculations in the mosaic lsm.
647 Tech. rep., NASA, Goddard Space Flight Center.
- 648 Koster, R., M. Suarez, A. Ducharne, M. Stieglitz, and P. Kumar, 2000: A catchment-based
649 approach to modeling land surface processes in a general circulation model. I- Model
650 structure. *Journal of Geophysical Research*, **105 (24)**, 809–24.
- 651 Koster, R. D., S. P. Mahanama, B. Livneh, D. P. Lettenmaier, and R. H. Reichle, 2010:
652 Skill in streamflow forecasts derived from large-scale estimates of soil moisture and snow.
653 *Nature Geoscience*, **3 (9)**, 613–616.
- 654 Lafaysse, M., 2011: Changement climatique et régime hydrologique d’un bassin alpin.
655 génération de scénarios sur la haute-durance, méthodologie d’évaluation et incertitudes
656 associées. Ph.D. thesis, Laboratoire d’Etude des Transferts en Hydrologie et Environ-
657 nement.
- 658 Liston, G., 2004: Representing subgrid snow cover heterogeneities in regional and global
659 models. *Journal of Climate*, **17 (6)**, 1381–1397.
- 660 Livneh, B., Y. Xia, K. E. Mitchell, M. B. Ek, and D. P. Lettenmaier, 2010: Noah LSM snow
661 model diagnostics and enhancements. *Journal of Hydrometeorology*, **11 (3)**, 721–738.
- 662 Loth, B. and H. Graf, 1998: Modeling the snow cover in climate studies 2. The sensitivity
663 to internal snow parameters and interface processes. *Journal of Geophysical Research*,
664 **103 (D10)**, 11 329–11.
- 665 Luce, C. and D. Tarboton, 2004: The application of depletion curves for parameterization
666 of subgrid variability of snow. *Hydrological Processes*, **18 (8)**, 1409–1422.
- 667 Luce, C. H., D. G. Tarboton, and K. R. Cooley, 1999: Sub-grid parameterization of snow
668 distribution for an energy and mass balance snow cover model. *Hydrological Processes*, **13**,
669 1921–2933.

670 Lundberg, A., I. Calder, and R. Harding, 1998: Evaporation of intercepted snow: measure-
671 ment and modelling. *Journal of Hydrology*, **206 (3)**, 151–163.

672 Lynch-Stieglitz, M., 1994: The development and validation of a simple snow model for the
673 GISS GCM. *Journal of Climate*, **7 (12)**, 1842–1855.

674 Marks, D., J. Dozier, and R. E. Davis, 1992: Climate and energy exchange at the snow
675 surface in the alpine region of the sierra nevada: 1. meteorological measurements and
676 monitoring. *Water Resources Research*, **28 (11)**, 3029–3042.

677 Masson, V., J. Champeaux, F. Chauvin, C. Meriguet, and R. Lacaze, 2003: A global
678 database of land surface parameters at 1-km resolution in meteorological and climate
679 models. *Journal of Climate*, **16 (9)**, 1261–1282.

680 Mielke, A. and T. Roubícek, 2003: A rate-independent model for inelastic behavior of shape-
681 memory alloys. *Multiscale Modeling & Simulation*, **1 (4)**, 571–597.

682 Ngo-Duc, T., J. Polcher, and K. Laval, 2005: A 53-year forcing data set for land surface
683 models. *J. Geophys. Res.*, **110**, D06 116.

684 Niu, G. and Z. Yang, 2007: An observation-based formulation of snow cover fraction and
685 its evaluation over large north american river basins. *Journal of Geophysical Research*,
686 **112 (D21)**, D21 101.

687 Parajka, J., G. Blöschl, et al., 2006: Validation of MODIS snow cover images over Austria.
688 *Hydrology and Earth System Sciences Discussions Discussions*, **3 (4)**, 1569–1601.

689 Picouet, C., 2012: PARTIE 3 : COMPARAISON DES DONNÉES SWE (OBSERVATIONS
690 AU SOL) ET SCA (MODIS) AU DROIT DES NRC. Tech. rep., EDF-DTG.

691 Pomeroy, J., D. Gray, K. Shook, B. Toth, R. Essery, A. Pietroniro, and N. Hedstrom, 1998:
692 An evaluation of snow accumulation and ablation processes for land surface modelling.
693 *Hydrological Processes*, **12 (15)**, 2339–2367.

694 Quintana-Seguí, P., et al., 2008: Analysis of near-surface atmospheric variables: Validation
695 of the SAFRAN analysis over France. *Journal of Applied Meteorology and Climatology*,
696 **47 (1)**, 92–107.

697 Reichle, R., R. Koster, G. De Lannoy, B. Forman, Q. Liu, S. Mahanama, and A. Touré,
698 2011: Assessment and enhancement of MERRA land surface hydrology estimates. *Journal*
699 *of Climate*, **24 (24)**, 6322–6338.

700 Riggs, G. A., D. K. Hall, and V. V. Salomonson, 2006: MODIS snow products users' guide
701 to Collection 5. *NASA GSFC*.

702 Roesch, A., M. Wild, H. Gilgen, and A. Ohmura, 2001: A new snow cover fraction
703 parametrization for the ECHAM4 GCM. *Climate dynamics*, **17 (12)**, 933–946.

704 Rutter, N., et al., 2009: Evaluation of forest snow processes models (snowmip2). *Journal of*
705 *Geophysical Research: Atmospheres (1984–2012)*, **114 (D6)**.

706 Sellers, P., et al., 1996: A revised land surface parameterization (SiB2) for atmospheric
707 GCMs. Part I: Model formulation. *Journal of Climate*, **9 (4)**, 676–705.

708 Sheffield, J., G. Goteti, and E. Wood, 2006: Development of a 50-year high-resolution global
709 dataset of meteorological forcings for land surface modeling. *Journal of Climate*, **19 (13)**,
710 3088–3111.

711 Slater, A., et al., 2001: The representation of snow in land surface schemes: Results from
712 PILPS 2 (d). *Journal of Hydrometeorology*, **2 (1)**, 7–25.

713 Stieglitz, M., A. Ducharne, R. Koster, and M. Suarez, 2001a: The impact of detailed snow
714 physics on the simulation of snow cover and subsurface thermodynamics at continental
715 scales. *Journal of Hydrometeorology*, **2 (3)**, 228–242.

716 Stieglitz, M., A. Ducharne, R. Koster, and M. Suarez, 2001b: The impact of detailed snow
717 physics on the simulation of snow cover and subsurface thermodynamics at continental
718 scales. *Journal of Hydrometeorology*, **2** (3), 228–242.

719 Strasser, U., M. Bernhardt, M. Weber, G. Liston, W. Mauser, et al., 2008: Is snow sublima-
720 tion important in the alpine water balance? *The Cryosphere*, **2** (1), 53–66.

721 Swenson, S. and D. Lawrence, 2012: A new fractional snow-covered area parameterization
722 for the community land model and its effect on the surface energy balance. *Journal of*
723 *Geophysical Research*, **117** (D21), D21 107.

724 Taylor, K. E., 2001: Summarizing multiple aspects of model performance in a single diagram.
725 *Journal of Geophysical Research: Atmospheres (1984–2012)*, **106** (D7), 7183–7192.

726 Verseghy, D., 1991: CLASS A Canadian land surface scheme for GCMs. I. Soil model.
727 *International Journal of Climatology*, **11** (2), 111–133.

728 Vidal, J.-P., E. Martin, L. Franchistéguy, M. Baillon, and J.-M. Soubeyroux, 2009: A 50-
729 year high-resolution atmospheric reanalysis over France with the SAFRAN system. *Inter-*
730 *national Journal of Climatology*, **30** (11), 1627–1644.

731 Wang, T., 2012: Développement et évaluation du modèle de surface ORCHIDEE : apport
732 pour la simulation des cycles de l’eau et du carbone aux hautes latitudes. Ph.D. thesis,
733 UNIVERSITE DE VERSAILLES SAINT-QUENTIN-EN-YVELINES.

734 Weedon, G., et al., 2011: Creation of the watch forcing data and its use to assess global
735 and regional reference crop evaporation over land during the twentieth century. *Journal*
736 *of Hydrometeorology*, **12** (5), 823–848.

737 Yang, Z.-L., R. E. Dickinson, A. Robock, and K. Y. Vinnikov, 1997: Validation of the
738 snow submodel of the biosphere-atmosphere transfer scheme with russian snow cover and
739 meteorological observational data. *Journal of climate*, **10** (2), 353–373.

List of Tables

740

741

742

743

744

745

746

747

748

749

750

751

752

753

754

755

756

- 1 Characteristics of each elementary catchment in the Upper Durance River watershed. There are six gauging stations in the Upper Durance watershed: U.A.S. is the upstream area at the gauging station and $\overline{Q_{obs}}$ is the mean observed discharge. SD stations are stations of snow depth measurements. W_{melt} is the parameter introduced to create the hysteresis in the SCD. 33
- 2 Characteristics of meteorological datasets used in this study. T, air temperature at 2m; Q, specific humidity; V, wind; LW, longwave radiation; and SW, shortwave radiation. Annual means of main variables are calculated over 1980-2009 for the Upper Durance watershed. 34
- 3 Main characteristics of the studied simulations. 'Multi-tile' configuration accounts for the different types of vegetation present in an elementary catchment according to ECOCLIMAP. 35
- 4 Comparison between the REF and HYST simulations and MODIS observations, end of snow-covered period, maximum annual SWE, and the correlation coefficient calculated for every year from August 2000 to July 2009 in catchment 3. 36

TABLE 1. Characteristics of each elementary catchment in the Upper Durance River watershed. There are six gauging stations in the Upper Durance watershed: U.A.S. is the upstream area at the gauging station and $\overline{Q_{obs}}$ is the mean observed discharge. SD stations are stations of snow depth measurements. W_{melt} is the parameter introduced to create the hysteresis in the SCD.

Catchment ID	Area (km ²)	U.A.S. (km ²)	$\overline{Q_{obs}}$ (m.s ⁻³)	Number of SD stations	Elevation (m)		Land cover fraction(%)			W_{melt} (kg.m ⁻²)
					mean	range	Forest	Grass	Bare soil	
1	662	548	13.0	12	2133	2675	23	32	45	400
2	296	-	-	4	2267	3125	17	31	53	400
3	723	723	11.6	10	2176	2465	29	37	34	300
4	501	2170	49.4	2	1880	2427	31	37	32	100
5	147	-	-	2	2539	1894	6	34	60	500
6	397	549	9.7	3	2093	2021	22	38	40	400
7	401	946	19.5	2	1902	2238	37	30	33	13
8	461	3582	76.3	-	1511	2215	35	45	20	13
UDR	3588	3582	76.3	35	2024	3298	37	36	27	-

TABLE 2. Characteristics of meteorological datasets used in this study. T, air temperature at 2m; Q, specific humidity; V, wind; LW, longwave radiation; and SW, shortwave radiation. Annual means of main variables are calculated over 1980-2009 for the Upper Durance watershed.

	SAFRAN	SPAZM	DuO
Variables	T,Q,V Rain and Snow LW↓ and SW↓	Tmin and Tmax Precipitation	T,Q,V Rain and Snow LW↓ and SW↓
Spatial resolution	8 km	1 km	1 km
Temporal resolution	hourly	daily	hourly
Availability	1959-2010	1955-2010	1959-2010
References	Quintana-Seguí et al. (2008)	Gottardi et al. (2012)	-
Annual means			
T (° C)	3.4	4.5	4.5
Precipitation (mm/an)	1022	1300	1300
Q (kg/kg)	$4.43 \cdot 10^{-3}$	-	$4.82 \cdot 10^{-3}$
V (m/s)	1.7	-	1.7
LW↓ (W.m ⁻²)	268	-	272
SW↓ (W.m ⁻²)	174	-	174

TABLE 3. Main characteristics of the studied simulations. 'Multi-tile' configuration accounts for the different types of vegetation present in an elementary catchment according to ECOCLIMAP.

Simulation label	Snow parameterization	W_{\min}	W_{melt}	Vegetation
REF	initial	13	-	multi-tile
REF200	initial	200	-	multi-tile
REF400	initial	400	-	multi-tile
REF600	initial	600	-	multi-tile
REF _{forest}	initial	13	-	100% forest
REF _{grass}	initial	13	-	100% grassland
REF _{bs}	initial	13	-	100% bare soil
HYST	hysteresis	13	calibrated	multi-tile
HYST _{forest}	hysteresis	13	calibrated	100% forest
HYST _{grass}	hysteresis	13	calibrated	100% grass
HYST _{bs}	hysteresis	13	calibrated	100% bare soil

TABLE 4. Comparison between the REF and HYST simulations and MODIS observations, end of snow-covered period, maximum annual SWE, and the correlation coefficient calculated for every year from August 2000 to July 2009 in catchment 3.

Year	DOY < 5%			Max SWE [kg.m ⁻²]		r ²	
	OBS	REF	HYST	REF	HYST	REF	HYST
2000-2001	314	298	314	535	527	0.86	0.84
2001-2002	298	306	306	99	124	0.92	0.94
2002-2003	290	290	298	267	267	0.85	0.80
2003-2004	305	313	313	348	359	0.92	0.85
2004-2005	298	290	290	69	97	0.83	0.89
2005-2006	306	282	306	181	186	0.91	0.88
2006-2007	298	306	306	63	146	0.90	0.91
2007-2008	313	289	313	193	226	0.93	0.94
2008-2009	322	290	322	369	376	0.89	0.87

List of Figures

757

758

759

760

761

762

763

764

765

766

767

768

769

770

771

772

773

774

775

776

777

778

779

780

781

782

1 a) Durance watershed elevations and dam locations. b) Upper part of the Durance watershed : delineation of elementary catchments used in the CLSM and locations of the gauging stations.

40

2 a) SCF time series extracted from MODIS images (MOD10A2) in catchment 3 from July 2003 to August 2006. Interruptions reflect the weeks when cloud cover was more than 10%. b) Rates of SCF (d^{-1}); accumulation rates are represented by red bars and ablation rates by blue bars. Mean accumulation and ablation rates are calculated over 2000-2011. Rates below $0.01 d^{-1}$ in absolute terms appearing in grey are considered to be 'neutral' and are not considered in calculating the means. Taking them into account for them does not change our overall conclusion.

41

3 MODIS SCF versus maximum mean snow depth observations in catchment 3 over eight days from April 2000 to March 2006. Reddish colors represent months when snow cover accumulation prevails; bluish colors depict months when snow cover ablation is most important. Neutral colors such as grey and beige represent months with either no snow or very little change in the snow-cover extent.

42

4 Histogram of observed SCF variation rates derived from MODIS images for the entire Upper Durance catchment. Mean accumulation and ablation rates (in red and blue, respectively) are calculated over 2000-2011. The central bin, corresponding to small absolute variation rates (below $0.01 d^{-1}$), appears in gray and is not accounted for to calculate the mean rates of accumulation/ablation written in red/blue. These small rates are not significant given the accuracy of MODIS images and keeping them does not change the difference between these two mean rates.

43

783	5	a) Initial snow cover depletion curve of the CLSM. b) New snow cover depletion curve with hysteresis. The path taken by the SCF with respect to SWE is shown in black for accumulation and in grey for ablation.	44
784			
785			
786	6	Snow cover depletion curves as a function of vegetation configuration in the CLSM in catchment 3 calculated from August 2003 and July 2004. a) The REF simulation accounts for different types of vegetation in catchment 3. b) The REF _{grass} simulation with 100% of grassland. c) The REF _{forest} simulation with 100% of forest. d) The REF _{bs} simulation with 100% of bare soil. W_{melt} in this catchment is equal to $300 \text{ kg}\cdot\text{m}^{-2}$.	45
787			
788			
789			
790			
791			
792	7	a) Annual hydrograph simulated by REF compared with observations of the mean monthly values calculated from August 1980 to July 2009 in catchment 3 (in red and blue, respectively). b) Comparison between daily simulated SCFs (red line) and maximum SCFs observed over eight days from MODIS images.	46
793			
794			
795			
796			
797	8	a) Comparison of annual hydrographs between simulation REF (red) and simulation HYST (blue) calculated over 1980-2009 in catchment 3. b) Comparison of SCF evolution between the same simulations and observations.	47
798			
799			
800	9	Taylor diagrams (Taylor 2001) showing the performances of simulations REF (empty triangles) and HYST (filled triangles) in the 6 gauged stations of the Upper Durance watershed of a) 10-day averaged runoff and b) maximum snow extent over 8 days compared to the MODIS images. The black square shows the location of the observations in the Taylor space. The distance between the simulation points (triangles) and the reference point (black square) represents the RMSE of the centered time series. The magnitude of relative biases is depicted by the size and direction of the triangles and the catchment numbers are indicated above them.	48
801			
802			
803			
804			
805			
806			
807			
808			

809 10 Changes of energy and hydrological variables caused by the hysteretic SCD in
810 catchment 3 and calculated over 1980-2009. Changes between the simulations
811 HYST and REF are depicted by orange bars. The other three bars (gray,
812 light and dark green) show the changes between the single-tile HYST and
813 REF simulations. The black line represents the surface weighted-mean of the
814 three single-tile changes.

49

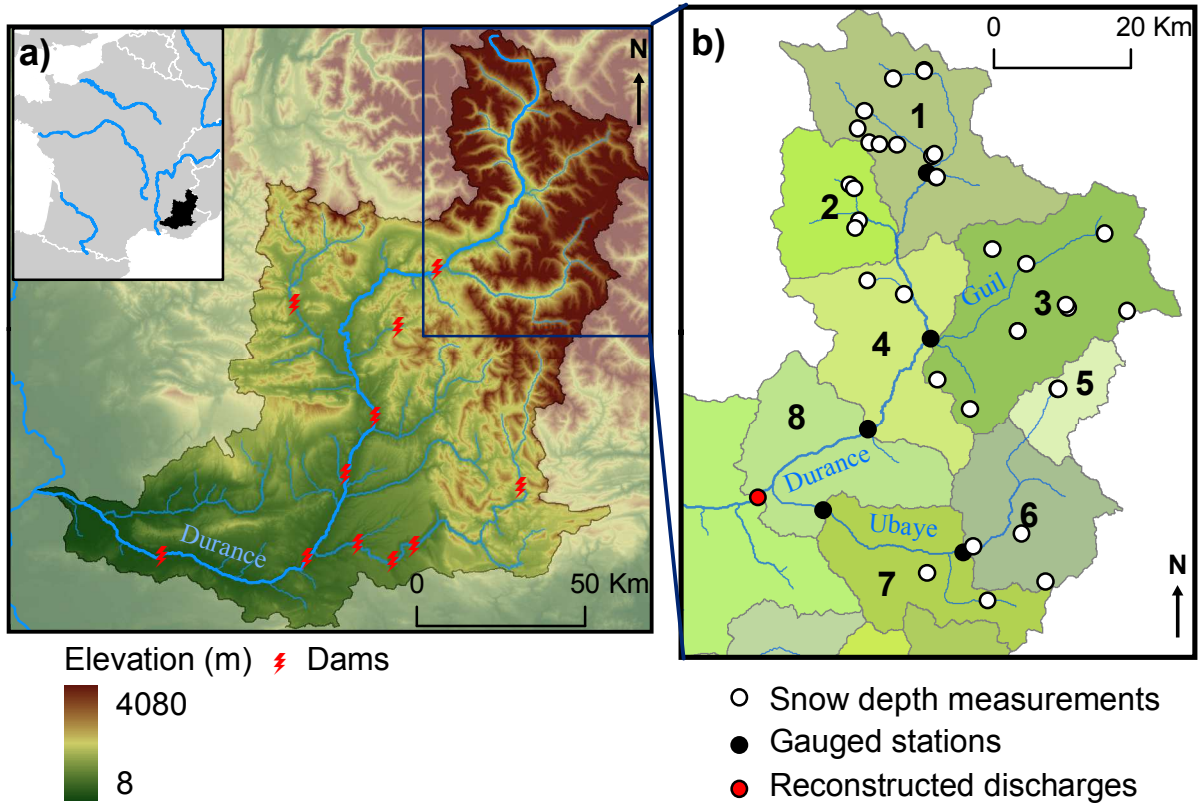


FIG. 1. a) Durance watershed elevations and dam locations. b) Upper part of the Durance watershed : delineation of elementary catchments used in the CLSM and locations of the gauging stations.

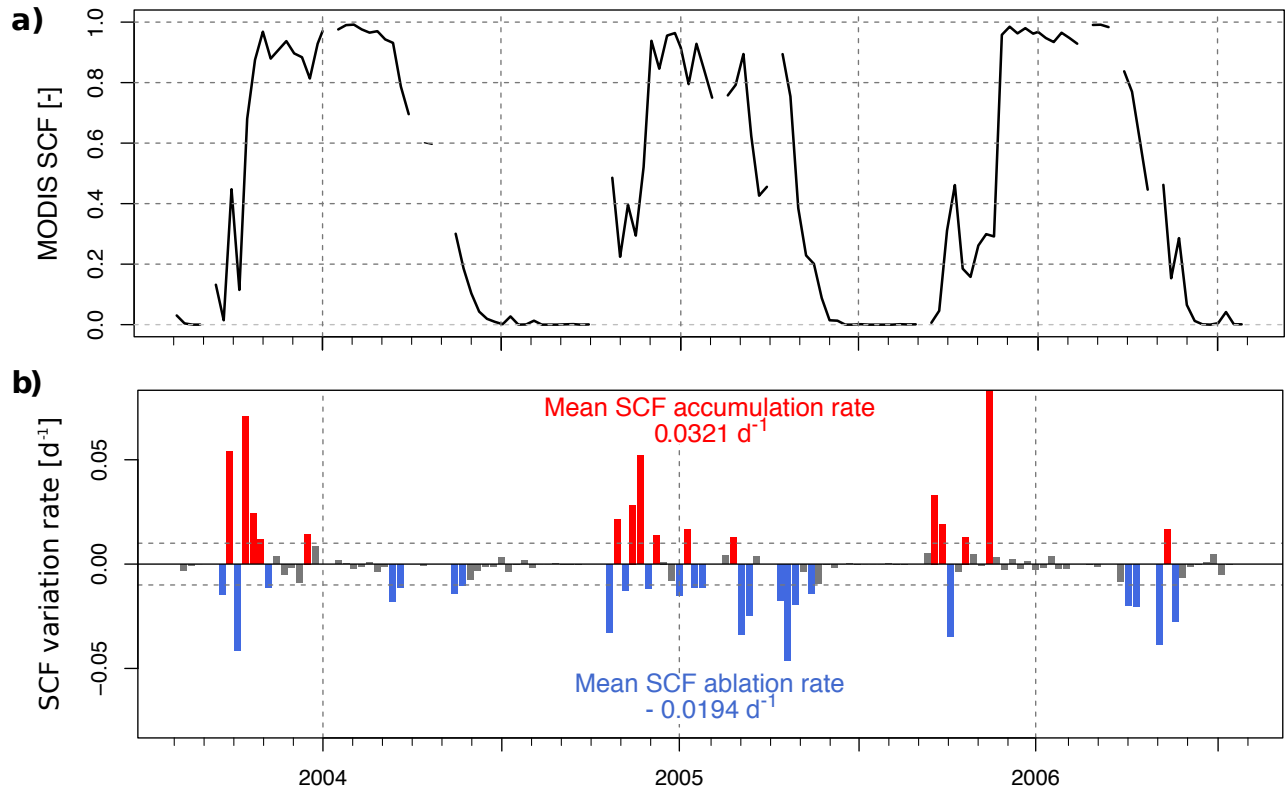


FIG. 2. a) SCF time series extracted from MODIS images (MOD10A2) in catchment 3 from July 2003 to August 2006. Interruptions reflect the weeks when cloud cover was more than 10%. b) Rates of SCF (d^{-1}); accumulation rates are represented by red bars and ablation rates by blue bars. Mean accumulation and ablation rates are calculated over 2000-2011. Rates below 0.01 d^{-1} in absolute terms appearing in grey are considered to be 'neutral' and are not considered in calculating the means. Taking them into account for them does not change our overall conclusion.

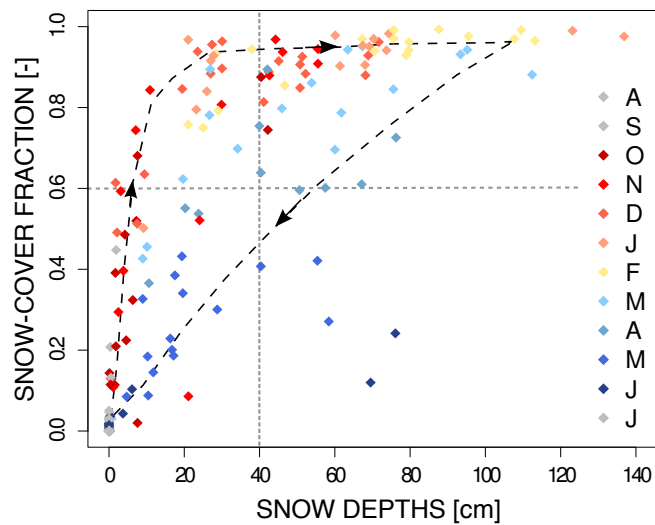


FIG. 3. MODIS SCF versus maximum mean snow depth observations in catchment 3 over eight days from April 2000 to March 2006. Reddish colors represent months when snow cover accumulation prevails; bluish colors depict months when snow cover ablation is most important. Neutral colors such as grey and beige represent months with either no snow or very little change in the snow-cover extent.

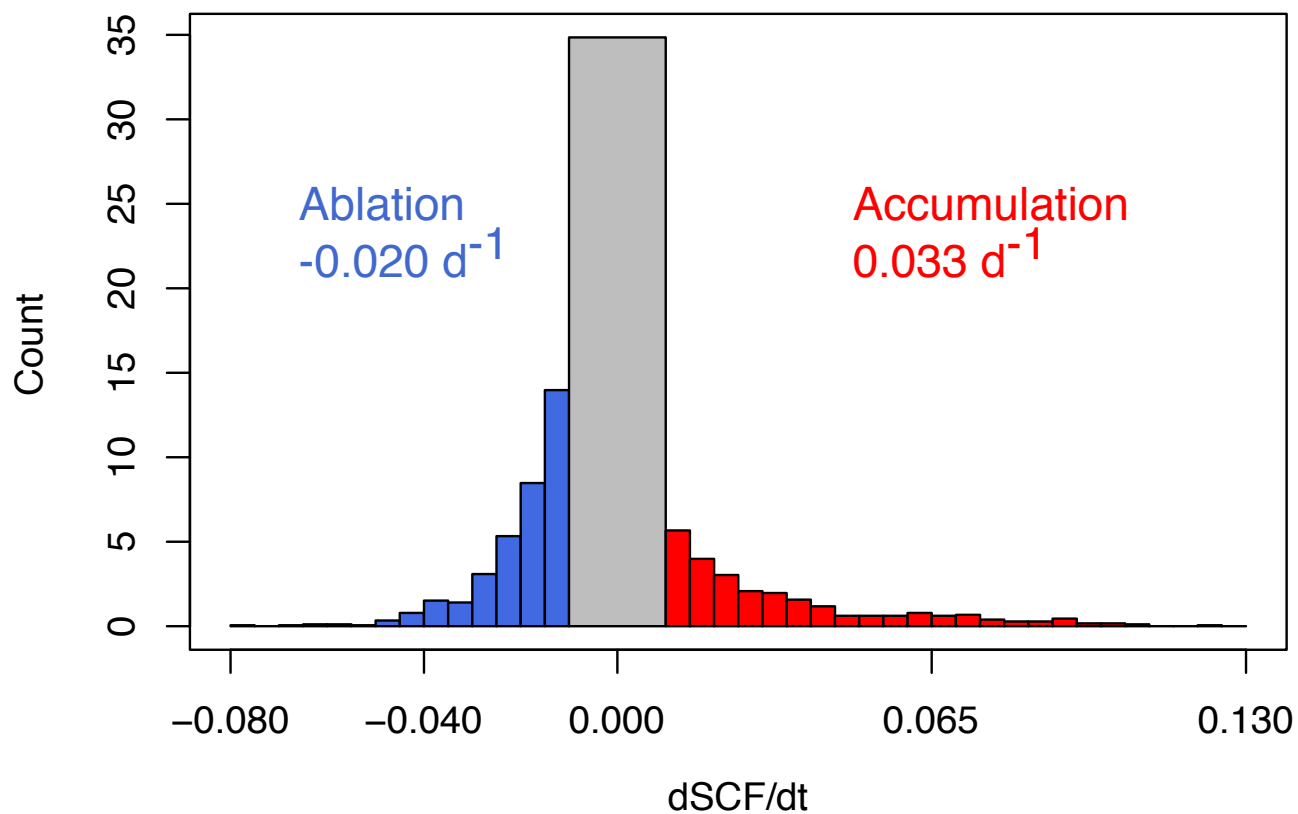


FIG. 4. Histogram of observed SCF variation rates derived from MODIS images for the entire Upper Durance catchment. Mean accumulation and ablation rates (in red and blue, respectively) are calculated over 2000-2011. The central bin, corresponding to small absolute variation rates (below 0.01 d^{-1}), appears in gray and is not accounted for to calculate the mean rates of accumulation/ablation written in red/blue. These small rates are not significant given the accuracy of MODIS images and keeping them does not change the difference between these two mean rates.

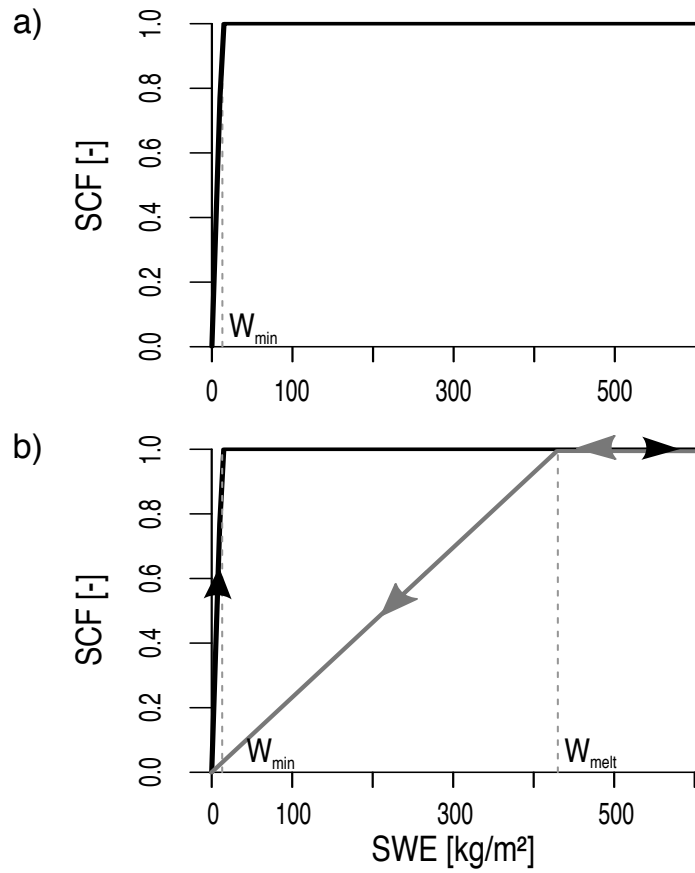


FIG. 5. a) Initial snow cover depletion curve of the CLSM. b) New snow cover depletion curve with hysteresis. The path taken by the SCF with respect to SWE is shown in black for accumulation and in grey for ablation.

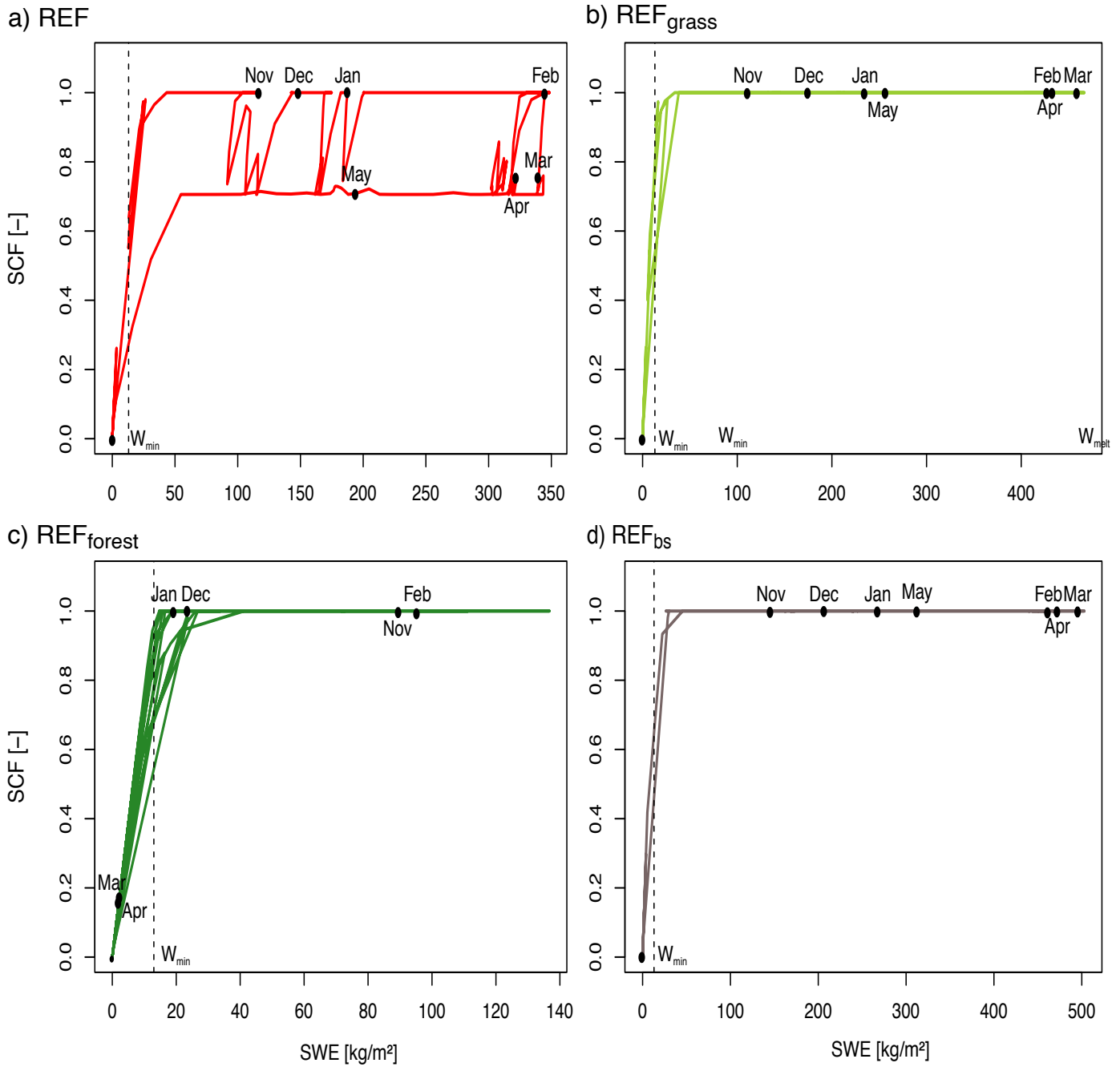


FIG. 6. Snow cover depletion curves as a function of vegetation configuration in the CLSM in catchment 3 calculated from August 2003 and July 2004. a) The REF simulation accounts for different types of vegetation in catchment 3. b) The REF_{grass} simulation with 100% of grassland. c) The REF_{forest} simulation with 100% of forest. d) The REF_{bs} simulation with 100% of bare soil. W_{melt} in this catchment is equal to $300 \text{ kg}\cdot\text{m}^{-2}$.

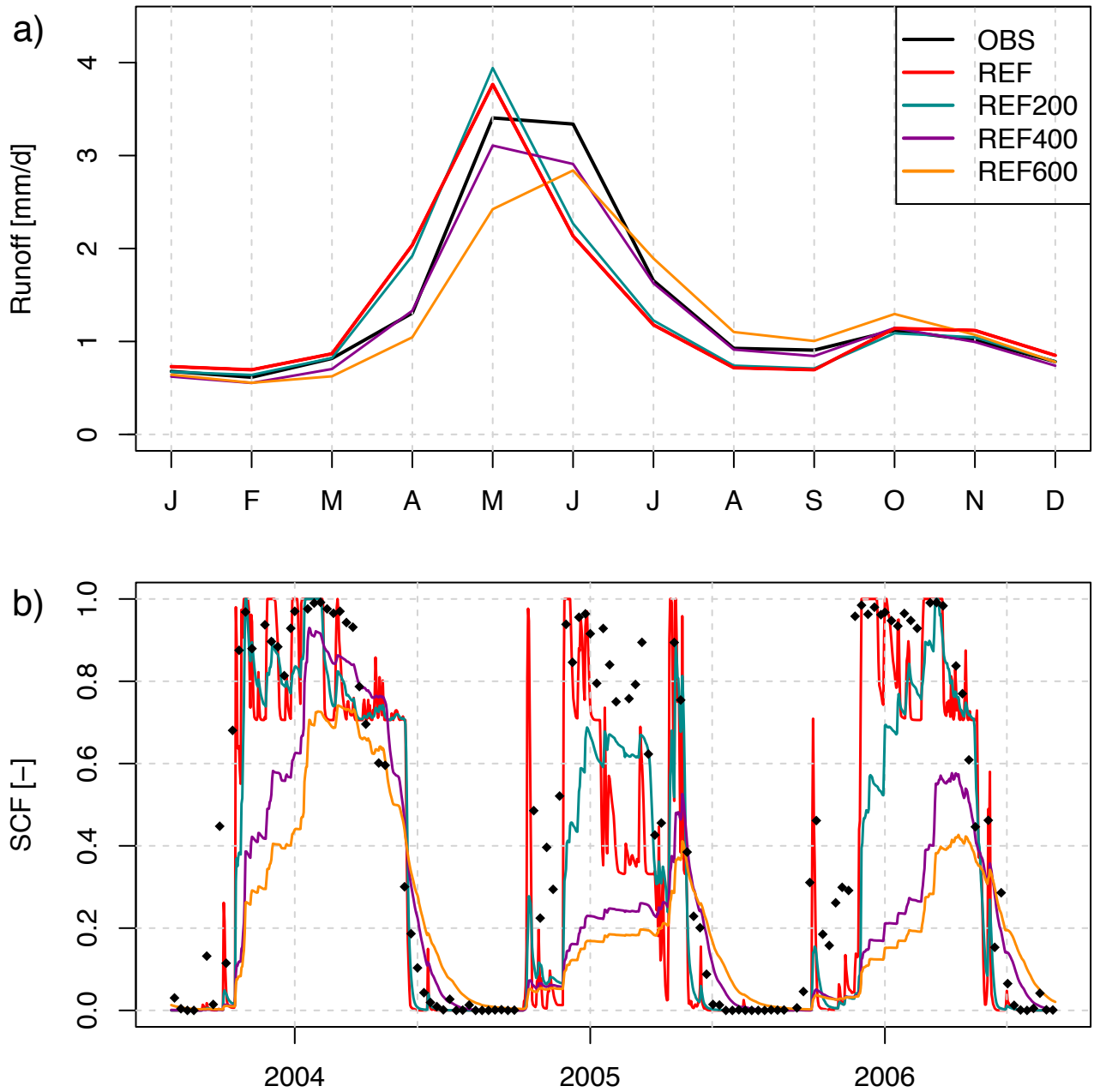


FIG. 7. a) Annual hydrograph simulated by REF compared with observations of the mean monthly values calculated from August 1980 to July 2009 in catchment 3 (in red and blue, respectively). b) Comparison between daily simulated SCFs (red line) and maximum SCFs observed over eight days from MODIS images.

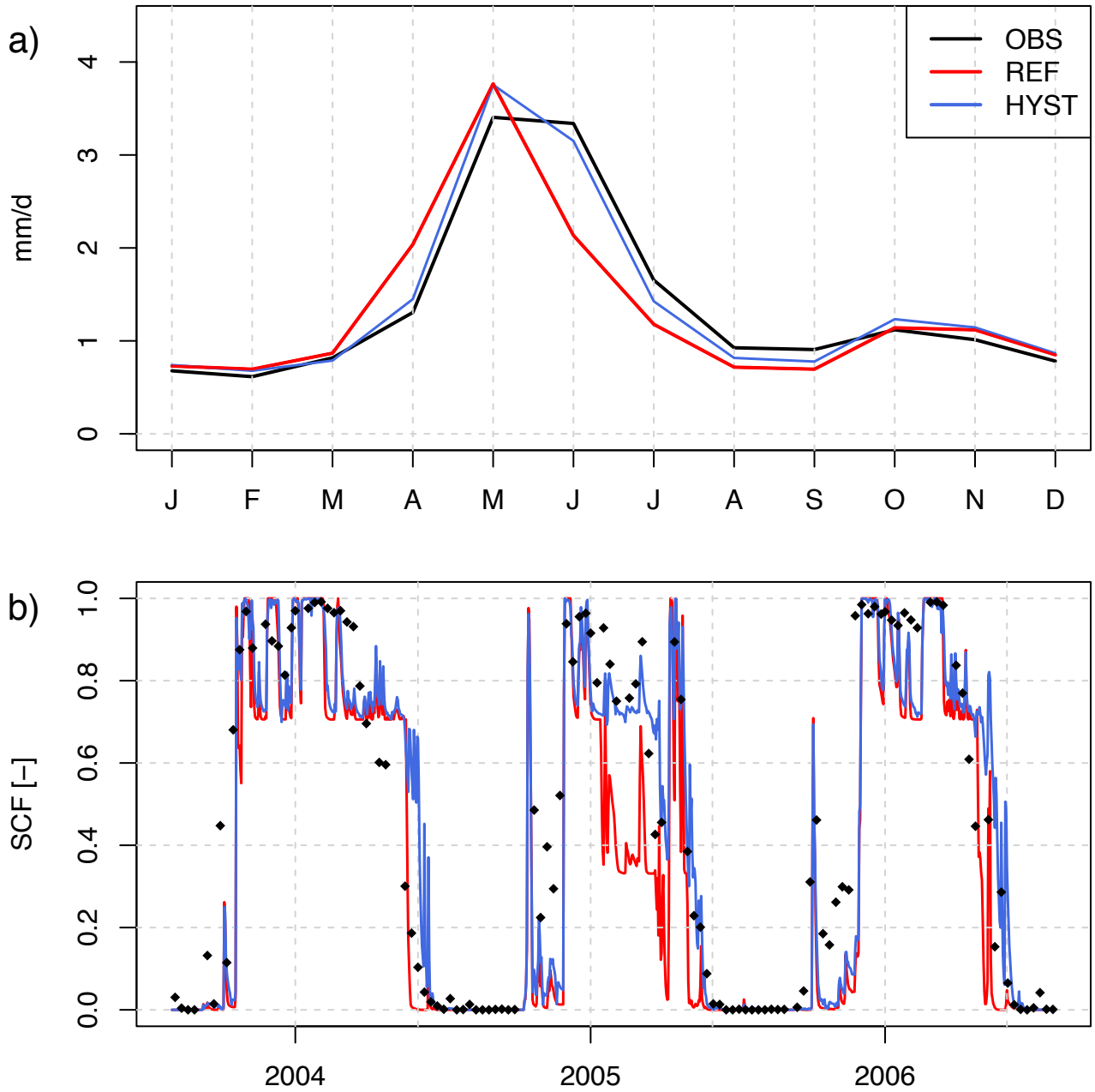


FIG. 8. a) Comparison of annual hydrographs between simulation REF (red) and simulation HYST (blue) calculated over 1980-2009 in catchment 3. b) Comparison of SCF evolution between the same simulations and observations.

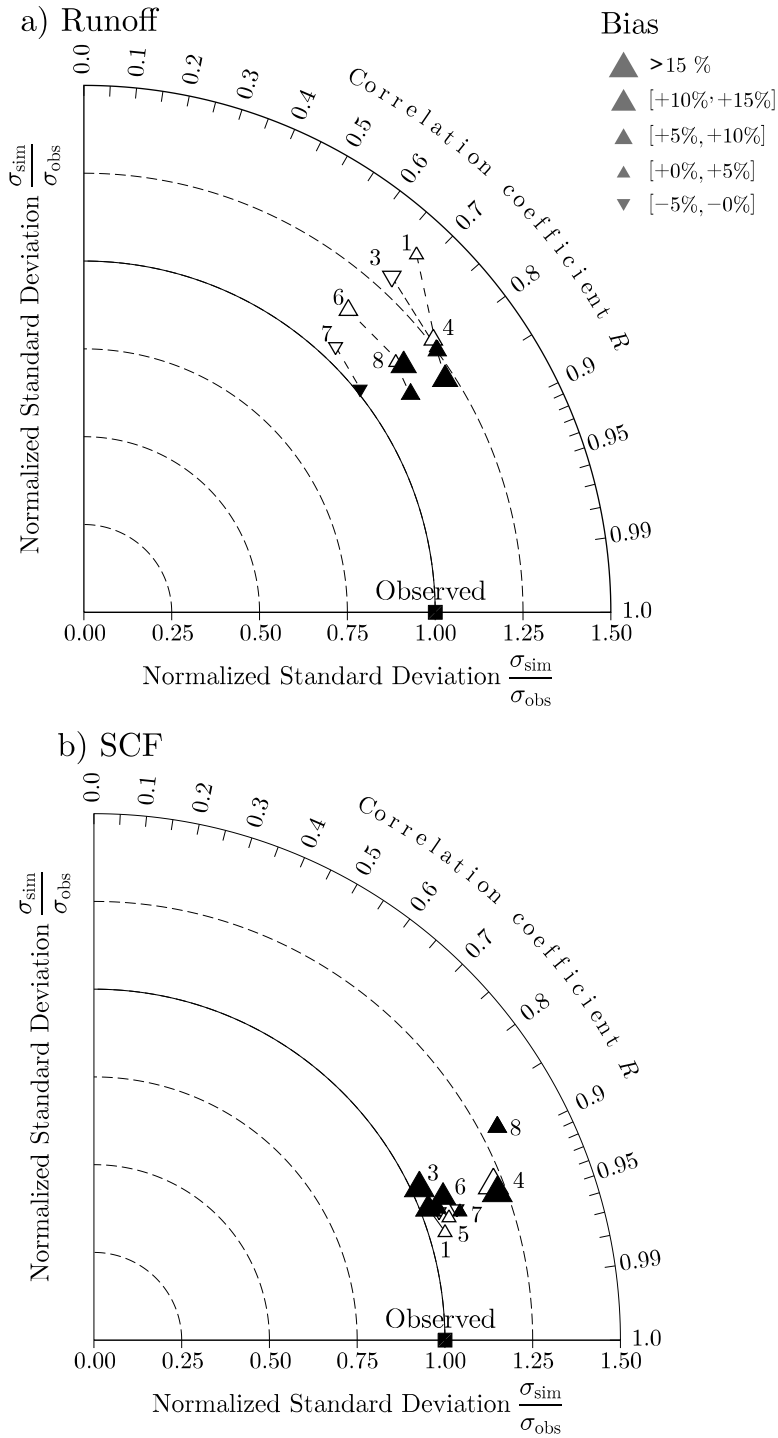


FIG. 9. Taylor diagrams (Taylor 2001) showing the performances of simulations REF (empty triangles) and HYST (filled triangles) in the 6 gauged stations of the Upper Durance watershed of a) 10-day averaged runoff and b) maximum snow extent over 8 days compared to the MODIS images. The black square shows the location of the observations in the Taylor space. The distance between the simulation points (triangles) and the reference point (black square) represents the RMSE of the centered time series. The magnitude of relative biases is depicted by the size and direction of the triangles and the catchment numbers are indicated above them.

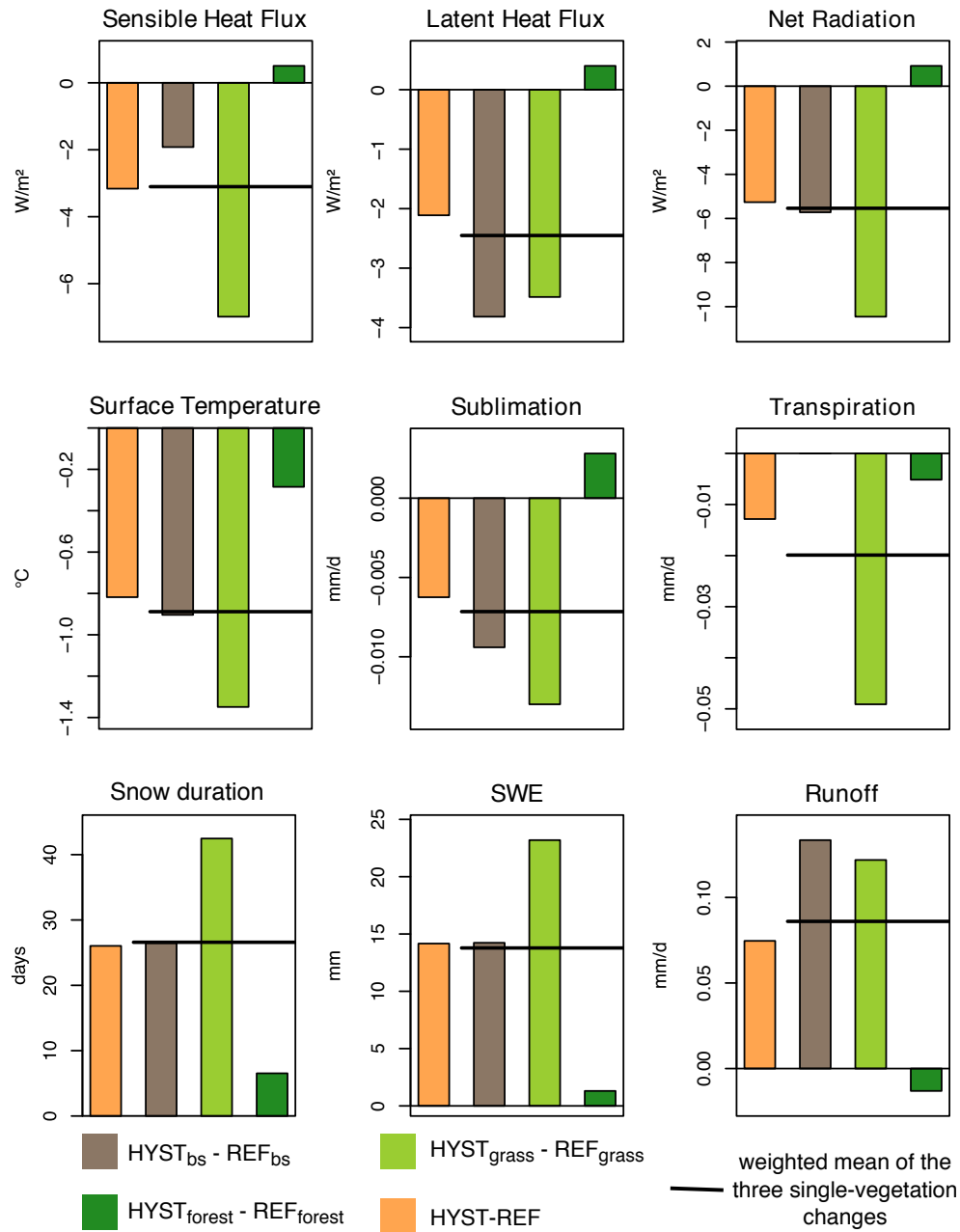


FIG. 10. Changes of energy and hydrological variables caused by the hysteretic SCD in catchment 3 and calculated over 1980-2009. Changes between the simulations HYST and REF are depicted by orange bars. The other three bars (gray, light and dark green) show the changes between the single-tile HYST and REF simulations. The black line represents the surface weighted-mean of the three single-vegetation changes.